

Non-neutralized Electric Current Patterns in Solar Active Regions: Origin of the Shear-Generating Lorentz Force

Manolis K. Georgoulis[†]

*Research Center for Astronomy and Applied Mathematics of the Academy of Athens
4 Soranou Efessiou Street, Athens, GR-11527, Greece*

and

Viacheslav S. Titov and Zoran Mikić

Predictive Science, Inc., 9990 Mesa Rim Road, San Diego, CA 92121, USA

ABSTRACT

Using solar vector magnetograms of the highest available spatial resolution and signal-to-noise ratio we perform a detailed study of electric current patterns in two solar active regions: a flaring/eruptive, and a flare-quiet one. We aim to determine whether active regions inject non-neutralized (net) electric currents in the solar atmosphere, responding to a debate initiated nearly two decades ago that remains inconclusive. We find that well-formed, intense magnetic polarity inversion lines (PILs) within active regions are the only photospheric magnetic structures that support significant net current. More intense PILs seem to imply stronger non-neutralized current patterns per polarity. This finding revises previous works that claim frequent injections of intense non-neutralized currents by most active regions appearing in the solar disk but also works that altogether rule out injection of non-neutralized currents. In agreement with previous studies, we also find that magnetically isolated active regions remain globally current-balanced. In addition, we confirm and quantify the preference of a given magnetic polarity to follow a given sense of electric currents, indicating a dominant sense of twist in active regions. This coherence effect is more pronounced in more compact active regions with stronger PILs and must be of sub-photospheric origin. Our results yield a natural explanation of the Lorentz force, invariably generating velocity and magnetic shear along strong PILs, thus setting a physical context for the observed pre-eruption evolution in solar active regions.

Subject headings: MHD — Sun: atmosphere — Sun: corona — Sun: flares — Sun: surface magnetism — Sun: photosphere

[†]Marie Curie Fellow.

1. Introduction

In spite of its relative thinness, the solar photosphere plays an important role as the transitional layer between the fluid-dominated solar interior and the magnetically dominated solar atmosphere. Over the past decades the emergence process of magnetic flux through the photosphere has been thoroughly studied by observers and modelers. An early observational finding was the filamentary, fibril structure of photospheric magnetic flux strands or tubes (e.g., Livingston & Harvey 1969; Howard & Stenflo 1972; Stenflo 1973) that defies the spatial resolution of our best magnetographs to this day. This fine, fibril structure of photospheric magnetic fields is yet to be fully understood and properly interpreted (Parker 1979, 2007).

Soon after the discovery of the filamentary photospheric magnetic fields, it was realized that emerging flux tubes must be twisted in order to maintain their structural integrity (Schuessler 1979). Recent simulations of magnetic flux emergence (Murray et al. 2006; Archontis & Hood 2008 and references therein) further showed that magnetic flux tubes cannot even emerge without some twist. Twist implies the presence of field-aligned electric currents, realized by the curl of the measured or simulated photospheric magnetic field vector per Ampere’s law. The existence of electric currents automatically implies departure of the magnetic structure from its minimum-energy, current-free (potential) configuration, as potential fields are defined by the gradient of a scalar potential calculated in a finite, bounded, or infinite, partly bounded, volume (Schmidt 1964; Sakurai 1982). Non-potentiality in solar magnetic fields is the undisputed underlying cause of solar eruptive activity originating typically in complex regions of interacting opposite-polarity magnetic fields, interfacing by strong polarity inversion lines (PILs). Observed photospheric PILs are typically deformed, shredded, and stretched by strong shear flows and associated magnetic shear, measured as the local angular difference between the observed field vector and the expected potential-field configuration (see, e.g., Wang (1999) for a review, but also Zirin & Wang (1993), Tiwari et al. (2010), and references therein).

In spite of strong mechanical forces and complexity in the photosphere, twist seems to remain almost unchanged in the corona (McClymont et al. 1997), where the substantially decreased plasma β -parameter allows for a nearly complete spatial filling of the coronal volume by magnetic field lines. The low- β coronal environment further implies almost purely field-aligned currents, except on thin current sheets that interface between flux tubes (Parker 1972, 2004). As a result, there is a *volume* current in flux tubes that is *non-neutralized* across any cross-section of the corona (e.g., Longcope & Welsch 2000). The notion of non-neutrality of electric currents implies the presence of a net (nonzero) current for a given magnetic polarity, as defined by previous works (e.g. Wilkinson et al. 1992; Wheatland 2000).

On the other hand, the presence of *volume* currents in twisted magnetic fibrils embedded

in a relatively field-free space occupied by fluid plasma, that is the assumed case for the photosphere, necessarily implies the existence of return (skin or sheath) *surface* currents at the boundaries of these photospheric fibrils (Pizzo 1986; Ding et al. 1987; Longcope & Welsch 2000). In addition to a field-aligned twist component, therefore, photospheric electric current density shows a significant component perpendicular to the magnetic field \mathbf{B} . This cross-field current density partially depends on $\nabla B \times \mathbf{B}$ -terms, caused by gradients of the magnetic field strength B (Zhang 2001; Georgoulis et al. 2004). As such, this component should peak on the surface of the flux tube where the interface between the magnetized and field-free mediums occurs. In the simplest case of isolated flux tubes it can be shown (see §5) that the Lorentz force due to these cross-field currents is mainly due to magnetic pressure (see, e.g., Jackson’s (1962) decomposition of the Lorentz force into pressure and tension terms) and tends to expand the flux tube, hence competing with the twist that keeps it together in conjunction with the external non-magnetized plasma pressure.

Little doubt exists that photospheric magnetic fields are indeed forced i.e., subjected to significant Lorentz forces (Metcalf et al. 1995; Georgoulis & LaBonte 2004). Above the photosphere, however, the plasma pressure decreases abruptly forcing flux tubes to expand rapidly to fill nearly the entire coronal volume, thus smoothing out large gradients ∇B . Because of this, return currents cannot reach the corona - they fade when magnetic fields become force-free (i.e., showing only a volume current due to the twist along the field). Details of this process remain to be determined, but an interesting mechanism relying on torsional Alfvén waves has been suggested by Longcope & Welsch (2000).

While it is generally established that a net electric current exists in any coronal cross-section, debate pertains over whether *photospheric* currents are neutralized. Parker (1996b) argued that for *isolated* magnetic fibrils embedded in a field-free volume, regardless of twist, the total current *must* be neutralized across the photospheric cross-section of any given flux tube. Simply, then, the vertical components of the volume and the surface currents cancel themselves in each fibril. Parker (1996b) further suggested that the common practice of inferring the vertical electric current density J_z via the differential form of Ampère’s law $(\nabla \times \mathbf{B})_z$ using photospheric magnetic field measurements \mathbf{B} bears no physical meaning. Thus, the presence of non-vanishing vertical currents in several observational cases is, according to Parker, an artifact caused by the limited spatial resolution of the observing magnetograph that tends to attribute an artificially continuous magnetic field where magnetic field is inherently discontinuous.

Melrose (1991; 1995) followed a different approach, by pointing out that observations are more consistent with non-neutralized photospheric current patterns. Therefore, currents have to emerge from the solar interior with the emergence of magnetic flux. That $\nabla \cdot \mathbf{J} = 0$

implies that currents have to close at the base of the convection zone (i.e., the tachocline) where magnetic fields are generated. This has profound implications for flare initiation: while Parker’s neutralized currents require in-situ storage and release of energy, Melrose’s large-scale current paths imply the existence of a strong inductive coupling between the coronal flaring volume and the convection zone. Melrose (1995) described magnetic loops as electric circuits (the $[\mathbf{E}, \mathbf{J}]$ -paradigm) and cited observations that showed an increase of magnetic shear after solar flares (Wang et al. 1994) to argue that the energy released in flares is replenished by pumping non-potential energy through electric currents from deep in the solar interior.

Parker (1996a) responded to Melrose’s proposition by arguing that the (\mathbf{E}, \mathbf{J}) -paradigm results in a set of dynamical equations that are mathematically intractable. In contrast, the magnetohydrodynamical (MHD) description of solar processes, in terms of a magnetic field \mathbf{B} and a velocity field \mathbf{u} (the $[\mathbf{B}, \mathbf{u}]$ -paradigm) is more natural and straightforward. The $[\mathbf{E}, \mathbf{J}]$ -paradigm may hold in laboratory conditions where magnetic fields are generated by current-carrying coils wrapped around metals, but not in stellar conditions where the dynamo-generated magnetic fields are the ones giving rise to electric currents.

A number of studies followed or preceded the debate, all focusing on its observational aspect, namely, whether there is non-neutralized current in the active-region photosphere meaning that net electric currents are injected into the atmosphere. The study of Wilkinson et al. (1992) was the only one to conclude that photospheric currents may be neutralized. All other studies (Leka et al. 1996; Semel & Skumanich 1998; Wheatland 2000; Falconer 2001) concluded that the active-region photosphere includes *current-carrying* magnetic flux tubes, although currents are roughly balanced at active-region scales, that is, non-neutralized currents of opposite senses close onto each other in a given active region. The inferred non-neutralized currents are interpreted as sub-photospheric in origin. Where these currents close, however, is unclear from observations and only Wheatland (2000) appeared to openly favor Melrose’s electric circuit analog. The above studies used both the differential form of Ampère’s law, that Parker (1996b) had criticized for failing to provide a physical current, and the integral form of Ampère’s law, i.e.,

$$I = \frac{c}{4\pi} \int_S (\nabla \times \mathbf{B}) \cdot \hat{\mathbf{n}} dS = \frac{c}{4\pi} \oint_C \mathbf{B} \cdot d\mathbf{l} \ , \quad (1)$$

where the total current I is obtained either over a cross-section S of a flux tube, where $\hat{\mathbf{n}}$ is the unit vector normal to S , or along a closed curve C bounding the cross-section S .

Although the expressions in equation (1) are equivalent (Stokes’ theorem), in practice numerical errors can give rise to notable uncertainties. First and foremost, the inference of magnetic field components via inversion of Stokes images and profiles includes uncertain-

ties subject to the specific inversion model (see, e.g., §1.3 of Borrero & Ichimoto (2011) and references therein). Because of these uncertainties and since different numbers of pixels are being used for the differential and the integral forms of equation (1), these uncertainties are different for the two theoretically equivalent expressions of Ampère’s law. The integral representation of Ampère’s law is often preferred because it involves fewer magnetogram pixels (i.e., the outline of a magnetic polarity, rather than the entire polarity used in the differential representation). Moreover, the azimuthal 180° -ambiguity, inherent in vector magnetic fields measured by the Zeeman effect (Harvey 1969), includes further uncertainties if incorrectly resolved. Further, magnetic field measurements are sometimes affected by Faraday rotation (Leka et al. 1996; Su et al. 2006) that is another source of uncertainties. When evaluating equation (1), finite differencing introduces truncation errors depending on the various differentiation schemes used, whereas the curve integral requires precise knowledge of the sequence of contiguous points on the bounding contour, regardless of this contour’s shape complexity.

The differential form of Ampère’s law gives rise to an electric current density $\mathbf{J} \sim \nabla \times \mathbf{B}$, of which only the vertical component J_z can be readily calculated in the photosphere. While calculation gives rise to large J_z -values, a valid question is whether these current density patterns are real. Leka et al. (1996) provide several interesting arguments supporting the realism of these currents. The most important is that in case of flux emergence, the increase in currents cannot be accounted for by the action of photospheric motions alone. In addition, patterns of the vertical current density J_z are known to reflect the expected morphology of the photospheric magnetic field (see, e.g., Socas-Navarro (2005) and Balthasar (2006), among others). This evidence, however, cannot be conclusive as $J_z \sim (\nabla \times \mathbf{B})_z$ should naturally reflect the shape of the field. McClymont et al. (1997), in their Appendix B, provided further physically-based arguments, namely that (i) the strongest non-neutralized currents occur in sunspots, where Parker (1996b) admits that the fibril state of the magnetic fields probably breaks down, (ii) inclined, spiral flux tubes cannot be maintained in their observed position without a true field-aligned current (i.e. twist) reflected in J_z , and (iii) J_z assumes a characteristic pattern along sheared magnetic polarity inversion lines (PILs), with narrow ribbon-like structures extending along both sides of the PIL. This, they argued, implies that the individual sheared flux strands are indeed blurred due to the insufficient instrumental resolution but, nonetheless, the current patterns are real, albeit smoothed and only partially resolved. An important conceptual step along the same lines was achieved by Semel & Skumanich (1998), who hinted that currents cannot be neutralized in case of *interacting* flux tubes with opposite polarities, that is, when a tight PIL interfaces between them. In this case one cannot argue for *isolated* flux fibrils, an apparent prerequisite for Parker’s neutralized currents.

Most of the above studies, including Parker’s, underlined the importance of studying

vector magnetograms with exceptionally high spatial resolution, sufficient to provide a better view of the fibril, discontinuous magnetic fields. The recent study of Venkatakrisnan & Tiwari (2009) uses an ultra-high-resolution vector magnetogram to conclude the absence of net currents in (isolated) sunspots, as Parker suggested. We also undertake this task here, but with a focus on (i) not restricting the analysis to isolated magnetic structures, and (ii) applying detailed error propagation to enable safe results and subsequent conclusions. We utilize two vector magnetograms obtained by the Spectro-Polarimeter of the Solar Optical Telescope onboard the *Hinode* spacecraft (Kosugi et al. 2007). As we shall see below, the spatial resolution and noise level of the *Hinode* magnetograms are unparalleled compared to magnetograms used in the previously cited studies of the 1990s. Therefore, these data are most appropriate and timely for the targeted sensitive calculations.

The data and preliminary analysis are described in §2. The methodology for calculating the total electric currents of “individual” (given the spatial resolution) flux tubes is outlined in §3. In §4 we present our results and in §5 we attempt a heuristic physical interpretation of them, connecting them with the observed evolution in the photosphere. We summarize our study and conclude in §6.

2. Vector magnetogram data processing

The Spectro-Polarimeter (SP; Lites et al. 2001) is part of the Solar Optical Telescope (SOT) package onboard the *Hinode* spacecraft. The instrument records the four Stokes polarization signals at the Fe I 6301.5 and 6302.5 Å photospheric magnetically sensitive spectral lines by scanning a portion of the solar disk with a spectral sampling of 21.6 $m\text{\AA}$. The normal scanning mode consists of 2048 steps at a nominal pixel spacing of 0.1585'' and with a full slit length equal to 1024 pixel lengths (Lites et al. 2008).

The inversion of the Stokes profiles is achieved via the Advanced Stokes Polarimeter (ASP) Milne-Eddington inversion code (Lites et al. (1993) and references therein). The inversion returns the magnetic field components with a 1σ sensitivity $\sigma B_l = 2.4 Mx cm^{-2}$ (G), for the line-of-sight field component, and $\sigma B_{tr} = 41 Mx cm^{-2}$, for the transverse field component. The full-resolution pixel size being 0.1585'', tests on quiet-Sun measurements revealed a spatial resolution of $\sim 0.3''$ (Lites et al. 2008). These can hardly be compared with pixel sizes of the order 1'' or lower (spatial resolution of the order 2'' or lower) and noise levels σB_l , σB_{tr} of the order several tens to 100-200 G, respectively, achieved by magnetographs used in the earlier studies of electric current patterns and their neutrality properties.

The resolution of the azimuthal 180° ambiguity in the selected *Hinode* vector mag-

netograms was achieved via the non-potential magnetic field calculation (NPFC) method of Georgoulis (2005), refined as discussed in Metcalf et al. (2006). The NPFC method is quite insensitive to noise (Leka et al. 2009) and performs well also in case of discontinuous and partially unresolved magnetic flux bundles (Georgoulis 2012), despite claims by Leka et al. (2009). The NPFC method is reliable enough to be the method of choice for the automatic disambiguation of vector magnetograms obtained by the Vector Spectromagnetograph (VSM) of the Synoptic Optical Long-Term Investigation of the Sun (SOLIS) facility (Georgoulis et al. 2008; Henney et al. 2009).

2.1. Hinode/SOT data on NOAA active region 10930

The first Hinode SOT/SP data set refers to NOAA active region (AR) 10930, a well-studied region observed on 2006 December 11. Figure 1a depicts a continuum image of the active-region photosphere, showing a clearly interacting δ -sunspot complex (i.e., interacting, opposite-polarity pattern including at least one strong PIL). The respective NPFC-disambiguated vector magnetogram is shown in Figure 1b. The scanning of the AR started at 13:53 UT and ended at 15:15 UT. Even from this single snapshot one notices the extreme magnetic shear ($\sim 90^\circ$) along the main PIL of the AR, whose area is selected and expanded in the inset of Figure 1b. Notice also the significant magnetic flux fragmentation everywhere in the field of view. Flux strands with cross-section of $\sim 1'' - 2''$ are abundant both close to the sunspots and to the extended plage areas surrounding them. The typical vertical field of these strands ranges between several hundred G and $\sim 1.5 kG$. Such fragmented field concentrations were first observed by the balloon-borne vector magnetograph onboard the Flare Genesis Experiment (pixel size $0.18''$; spatial resolution $\sim 0.5''$ - Bernasconi et al. 2002), but could only be guessed in previous studies (see, for example, Zirin (1988) for a collection of sunspot groups with notable fibril structure observed in $H\alpha$ wavelengths). Adjacent to the PIL (inset), one notices flux bundles, aligned with the PIL with a width as small as $\lesssim 2''$. These “channels” or “lanes” were first reported by Zirin & Wang (1993) and were exemplified by Wang et al. (2008) for this particular active region. The total field strength of these flux bundles is $\sim 2 kG$, with a vertical component $|B_z| \sim 1.5 kG$. The vertical field component on the PIL dropping precipitously to zero, the horizontal field shows an amplitude $B_h \sim (1.5 - 1.9) kG$.

Clearly, NOAA AR 10930 does not comply with the Hale-Nicholson polarity law (e.g. Zirin 1988): the leading/trailing polarity pattern is unclear and the AR axis shows a North-South, rather than an East-West, orientation. Given the extremely sheared PIL on the other hand, it is not surprising that the AR, during its passage from the visible disk (i.e., between

12/06/06 and 12/18/06) gave an impressive series of flares (3 X-class, 2 M-class, about a dozen C-class, and ~ 100 B-class events). The most intense of these flares, a GOES X3.4, took place at 02:14 UT on 2006 December 13, ~ 1.5 days after the Hinode observations of Figure 1.

A map of the vertical electric current density J_z is shown in Figure 1c, with the J_z -solution for the PIL expanded and shown in the inset. A brief look at the J_z -map roughly confirms the expected fine structure: in the penumbrae of both sunspots and away from the PIL there are roughly radial structures in agreement with previous studies (for example, Semel & Skumanich (1998); Balthasar (2006), and others). Further, in a secondary PIL north of the negative-polarity sunspot there are paired upward/downward J_z -patterns along the PIL. Along the AR's main PIL (inset) the strong shear indeed creates "tongue"-like upward and downward current patterns. Finally, the J_z -signature of the extended plage fields is much weaker, noisier, and lacks a coherent structure, that is evidence of magnetic fields nearly normal to the photosphere in these areas (Martinez Pillet et al. 1997).

Overall, the vertical electric current density solution for NOAA AR 10930 shows striking fine structure. Magnetic flux fragmentation easily reaches down to the spatial-resolution capability of the observing instrument. Therefore, we cannot claim that the observed magnetic configuration is fully resolved. The observed J_z -structure might, in fact, be what McClymont et al. (1997) argued for, namely, the result of multiple unresolved magnetic fibrils that are imperfectly observed as a single flux tube.

2.2. Hinode/SOT data on NOAA active region 10940

The second data set pertains to Hinode's SOT/SP observations of NOAA AR 10940, observed on 2007 February 2. The scanning of the AR started at 01:50 UT and ended at 02:53 UT. Figure 2a shows a continuum photospheric image of the AR. From this image, the AR consists of a fairly undisturbed sunspot surrounded by extended plage and a number of smaller spots, or pores. Evidence for a small emerging flux sub-region exists just west of the main sunspot, where the continuum image shows dark fibril structures such as those expected in arch filament systems (Bruzek 1967). This area is expanded and shown in the inset. The PIL of the AR is in the same area but is much weaker than the main PIL of NOAA AR 10930. The NPFC-disambiguated solution for the heliographic magnetic field vector is shown in Figure 2b. The horizontal field vector shows the typical radial arrangement expected for an undisturbed sunspot while some weak shear can be seen along the PIL.

The solution for the vertical current density, shown in Figure 2c, is also enlightening: the

sunspot’s penumbra generally exhibits radial J_z -patterns except close to the PIL, where these patterns are deformed (inset). There, the J_z -patterns roughly follow the orientation of the dark fibrils of the arch filament system as seen in the continuum (Figure 2a). Weak, plage, J_z -patterns can also be seen, while the small radial pattern in the westernmost part of the AR indicates that the darkening in the continuum image and the coherent negative-polarity feature in the vector-field image correspond to a small sunspot with almost no umbra. In this example, too, the J_z -patterns provide physical information on the studied AR. As such, they may not be completely artificial.

The NOAA AR 10940 is much more quiescent compared to NOAA AR 10930 of Figure 1. During its passage from the visible disk (\sim 01/28 - 02/09 2007) the AR gave only 3 weak C-class flares and \sim 25 B-class events. At the time of the Hinode observations on February 2, the AR was almost totally flare-quiet.

We seek the qualitative and quantitative differences between the electric current patterns in the two ARs. The findings will be used to determine, using the highest possible spatial resolution, whether current-injecting magnetic flux tubes are widespread, rarely occurred, or simply non-existent.

3. The analysis method

To calculate the total electric current in an entire active region or in polarities of it, we take the following steps: first, we translate the pixelized photospheric magnetic-flux distribution into a collection of partitions, each with a relatively large ($\gg 1$) number of pixels. Second, we apply the integral form of Ampère’s law [Equation (1)] to these partitions to calculate their total electric current. Third, we algebraically sum the total currents of all partitions to calculate the total current of each polarity and of the entire region.

Alternatively, the total current can be obtained by, first, deriving the normal component J_z of the electric current density from a vector magnetogram and then integrating the J_z -distribution over the area of a given partition with N pixels or the active region as a whole. Calculating the total current from the integral Ampere’s law does not rely on the current densities of all N pixels of a studied partition but it uses the magnetic field components of only $\sim \sqrt{N}$ pixels - those that belong to the perimeter of the partition. Choosing a sufficiently high magnetic-field threshold in the outline of the partitions we achieve a relatively high signal-to-noise ratio, and hence a reasonable uncertainty in our calculations.

3.1. Magnetic flux partitioning

Photospheric flux partitioning is achieved following the partition method of Barnes et al. (2005). Partitioning the vertical component B_z of a magnetogram \mathbf{B} aims to “discretize” the otherwise continuous magnetic flux distribution, by translating it into a series of well-defined, non-overlapping partitions of different polarities with uniquely defined outlines, areas, and flux contents. Numerically, our method of choice is a “gradient-based” flux tessellation scheme that uses a downhill-gradient algorithm (e.g. Press et al. 1992) to define photospheric partitions based on the two-dimensional morphological and polarity characteristics of B_z . In addition, a simplification rule is applied, merging partitions that interface by saddle points in B_z .

If no thresholds were imposed in the course of partitioning, the entire magnetogram area, including active-region and quiet-Sun patches, would be included in an excessive number of different partitions. It is of little meaning, however, to include weak and/or tiny partitions from the highly fragmented Hinode magnetograms, as these partitions are unlikely to contribute strong currents. For this reason, we focus on strong-flux active-region patches by defining relatively high thresholds for the basic parameters of partitioning: (i) $B_{z_{thres}} = 100\text{ G}$ as the minimum B_z -value for each pixel of a given partition, (ii) $\Phi_{thres} = 10^{19}\text{ Mx}$ as the minimum magnetic flux Φ of a partition, and (iii) $S_{thres} = 40\text{ pixels}$ as the minimum partition area S . A partition qualifies for further study only if *all* three thresholds are exceeded; otherwise, it is discarded.

A slight mean-neighborhood smoothing is also applied to the original B_z -maps in order to reduce an excessive jaggedness of the partition contours. Once these contours are determined, however, the original, non-smoothed maps of the horizontal field components are used to calculate the total currents.

3.2. Calculation of the total electric current and uncertainties

3.2.1. For individual magnetic flux partitions within active regions

Discretizing the integral Ampère’s law [Equation (1)], we obtain for each qualifying partition i the total current

$$I_i = \frac{c\lambda}{4\pi} \sum_{k=1}^{K_i} (B_{x_k} \Delta x_k + B_{y_k} \Delta y_k), \quad (2)$$

where λ is the pixel size in physical units and K_i is the number of pixels along the contour C_i of the partition. Each k -th pixel of the contour is characterized by a horizontal magnetic

field $\mathbf{B}_{h_k} = B_{x_k} \hat{\mathbf{x}} + B_{y_k} \hat{\mathbf{y}}$ and a vector $\Delta \mathbf{l}_k = \Delta_{x_k} \hat{\mathbf{x}} + \Delta_{y_k} \hat{\mathbf{y}}$, whose components assume one of three possible values (0, +1, and -1) and represent the unit displacement along the contour.

A practical issue is the specification of the sequence of contiguous points that comprise the bounding contour $\Delta \mathbf{l}$ of a partition. For this we use an “edge tracker” algorithm introduced by Georgoulis et al. (2012). The algorithm minimizes the length of the curve by iteratively selecting pairs of adjacent contour points. Contour-length minimization is achieved by a simulated annealing method (Press et al. 1992).

From Equation (2), we can estimate the corresponding uncertainty δI_i of I_i . We assume that δI_i stems only from the uncertainties δB_{x_k} and δB_{y_k} of the field components B_{x_k} and B_{y_k} , respectively, while Δ_{x_k} and Δ_{y_k} are known without uncertainties. Considering also δB_{x_k} and δB_{y_k} to be independent from each other, we obtain from Equation (2)

$$\delta I_i = \frac{c\lambda}{4\pi} \sqrt{\sum_{k=1}^{K_i} (\Delta_{x_k}^2 \delta B_{x_k}^2 + \Delta_{y_k}^2 \delta B_{y_k}^2)}. \quad (3)$$

If B_{x_k} and B_{y_k} are the horizontal heliographic field components on the image (observer’s) plane, then their uncertainties, δB_{x_k} and δB_{y_k} , respectively, can be calculated by implementing the analytical method described in Appendix I of Georgoulis & LaBonte (2004). We use this approach in the following.

Thus, for each partition i we calculate the total electric current I_i from Equation (2) and its uncertainty δI_i from Equation (3). As a sanity check, Equation (2) is also used to calculate the total electric current I'_i using a *potential* magnetic field vector calculated from the disambiguated solution of the photospheric B_z -distribution. An exact potential field implies that $I'_i \equiv 0$ for every i . However, due to various numerical effects, all I'_i show a nonzero value. Comparison between I_i and I'_i can help assess the significance of the nonzero total current I_i of a given partition i and hence the non-neutrality of this partition.

To calculate the photospheric potential field \mathbf{B}_p from a given photospheric B_z distribution, we apply the analytical Green’s function method proposed by Schmidt (1964). This method is much slower, but quite more accurate - for a given choice of boundary conditions - than the numerical fast-Fourier-transform method of Alissandrakis (1981). In the analytical method we assume $\mathbf{B}_p = -\nabla\psi$, where ψ is a smooth scalar potential, i.e.,

$$\psi(\mathbf{r}) = \frac{1}{2\pi} \int \int \frac{B_z(\mathbf{r}')}{|\mathbf{r} - \mathbf{r}'|} dx' dy' \quad , \quad (4)$$

defined at a given point $\mathbf{r} = x\hat{\mathbf{x}} + y\hat{\mathbf{y}}$ of the photospheric plane. B_z , on the other hand, is a known function of position $\mathbf{r}' = x'\hat{\mathbf{x}} + y'\hat{\mathbf{y}}$ ($\mathbf{r} \neq \mathbf{r}'$).

Taking into account the above uncertainties, we characterize a given partition i as *non-neutralized* if

$$|I_i| > 5 |I'_i| \text{ and } |I_i| > 3 \delta I_i. \quad (5)$$

In other words, we impose a 5σ significance level toward the total currents I'_i of the potential field *and* a 3σ significance level toward the calculated uncertainties δI_i .

3.2.2. For active regions as a whole

In an given active region, let N be the number of qualifying partitions per the criteria of §3.1, and Φ_i, I_i be the magnetic flux and total current, respectively, of a given partition i . The total currents I_+ and I_- of the positive and negative polarities, respectively, of the region are then given by (e.g. Wheatland 2000)

$$\begin{aligned} I_+ &= \sum_{i=1}^N s_i^+ I_i, & \text{where } s_i^+ &= \frac{1}{2} \left[1 + \frac{\Phi_i}{|\Phi_i|} \right], \\ I_- &= \sum_{i=1}^N s_i^- I_i, & \text{where } s_i^- &= \frac{1}{2} \left[1 - \frac{\Phi_i}{|\Phi_i|} \right], \end{aligned} \quad (6)$$

with uncertainties

$$\delta I_+ = \left(\sum_{i=1}^N s_i^+ \delta I_i^2 \right)^{1/2}, \quad (7)$$

$$\delta I_- = \left(\sum_{i=1}^N s_i^- \delta I_i^2 \right)^{1/2}. \quad (8)$$

Evidently, significant (i.e., sufficiently larger than applicable uncertainties) I_+, I_- imply non-neutralized currents for the respective polarities. Moreover, the net current in the AR is given by

$$I_{\text{net}} = \sum_{i=1}^N I_i = I_+ + I_- \quad (9)$$

and has an uncertainty

$$\delta I_{\text{net}} = \left(\sum_{i=1}^N \delta I_i^2 \right)^{1/2} = \sqrt{\delta I_+^2 + \delta I_-^2}. \quad (10)$$

The solar plasma is considered electrically neutralized, since all the physical processes in the Sun are relatively slow. Then, the conservation of the electric charge in the solar

atmosphere implies that the electric current density \mathbf{J} must be solenoidal, i.e. $\nabla \cdot \mathbf{J} = 0$. In integral form, this means that the net current through any closed surface, such as the photosphere, must be zero. Taking into account that the strongest coronal magnetic fields and so the currents are localized within solar ARs, we expect that magnetically isolated ARs should be current-balanced ($I_{net} \sim 0$). In practice, however, there may be large-scale magnetic connections between the AR and its surroundings, so the net current may be different from zero. This may also happen if the observed area does not include the entire AR.

To jointly characterize imbalances of the total current and the magnetic flux in a given AR, we introduce the following dimensionless parameters: the electric-current imbalance and the magnetic-flux imbalance, \mathcal{I}_{imb} and \mathcal{F}_{imb} , respectively, where

$$\mathcal{I}_{imb} = \frac{|I_{net}|}{\sum_{i=1}^N |I_i|}, \quad (11)$$

$$\mathcal{F}_{imb} = \frac{|\Phi_+ + \Phi_-|}{\Phi_+ - \Phi_-}. \quad (12)$$

Here $\Phi_+ = \sum_{i=1}^N s_i^+ \Phi_i$ and $\Phi_- = \sum_{i=1}^N s_i^- \Phi_i$ are the total magnetic fluxes in the positive and negative polarities of the AR, respectively. We will consider the currents in a given AR to be balanced if the inequality

$$\mathcal{I}_{imb} \ll \mathcal{F}_{imb} \quad (13)$$

is satisfied. This means that the smaller the ratio $\mathcal{I}_{imb}/\mathcal{F}_{imb}$ (ideally $\mathcal{I}_{imb} \ll \mathcal{F}_{imb} \ll 1$), the more confident we are that the AR is current-balanced.

If the criterion of Equation (13) is satisfied, it is also meaningful to obtain a uniform, normalized degree of neutrality (or non-neutrality, thereof) within *each* polarity of the AR. For this purpose we introduce the global (current) non-neutrality factor

$$\mathcal{I}_{nn}^\pm = \frac{1}{2} \left(\frac{|I_+|}{\sum_{i=1}^N |s_i^+ I_i|} + \frac{|I_-|}{\sum_{i=1}^N |s_i^- I_i|} \right). \quad (14)$$

This dimensionless parameter determines the degree to which different partitions of the same polarity show the same sense of total electric current. For strongly non-neutralized, but also *coherent* polarities, whose partitions predominantly show a given sense of non-neutralized total current, one obtains $\mathcal{I}_{imb} \ll \mathcal{I}_{nn}^\pm \sim 1$. For very incoherent, or current-neutralized, polarities, $\mathcal{I}_{imb} \sim \mathcal{I}_{nn}^\pm \ll 1$. The intermediate cases $\mathcal{I}_{imb} \ll \mathcal{I}_{nn}^\pm < 1$ and $\mathcal{I}_{imb} < \mathcal{I}_{nn}^\pm < 1$ imply a degree of incoherence and/or non-neutrality for each polarity.

4. Current patterns in the selected ARs

4.1. NOAA AR 10930

Figure 3a shows the flux-partitioned vertical magnetic field of NOAA AR 10930. We identified a total of $N = 531$ flux partitions, of which $p = 246$ show positive polarity and $n = 285$ show negative polarity. To cross-check our calculation, we infer the mean vertical electric current density of each partition in two different ways: first, by dividing the total current I_i of each partition i by the area S_i of the partition ($J_{z_i} = I_i/S_i$) and, second, by averaging all the local vertical current densities J_{z_q} within each partition i ($J_{z_i} = \langle J_{z_q} \rangle$), where J_{z_q} have been obtained from the differential expression of Ampère’s law. Close correlation between these two J_z -maps implies precise calculation of the bounding contours of the partitions. The results from the two mean- J_z calculations are depicted in Figures 3c and 3d, respectively, and are compared in Figure 3b. Evidently there is close agreement between the two alternative current density calculations. The generally small discrepancies are mostly caused by uncertainties in the calculation of the differential J_{z_q} via finite differencing. This action is expected to slightly overestimate the magnitudes $|J_{z_i}|$ of the differential J_{z_i} . Indeed, Figure 3b shows $(J_z)_{integral} \sim 0.94(J_z)_{differential}$, implying a flatter least-squares best fit (black line) than the analytical equality (red line).

We now focus on the total electric currents of individual partitions. In random order, these currents appear in Figure 4a. We also check which of these currents survive our significance test of equations (5). Notably, 120 of the 531 identified partitions satisfy the significance criteria. Of them, however, only ~ 25 have strong enough total currents to be discernible in Figure 4a (non-neutralized currents shown with red columns and green error bars). Regardless, it is evident that *there are* flux partitions in the AR with non-neutralized currents. What is more instructive is the spatial distribution of these partitions, shown in the detail of Figure 4b. We find that partitions with the strongest non-neutralized currents are *adjacent* to the PILs of the AR. The two main interacting sunspots (labeled 1 and 2 in Figures 4a and 4b) have large total currents with values $\sim 45 \times 10^{11} A$ and $\sim -35 \times 10^{11} A$, respectively. Partitions adjacent to the secondary PILs of the AR, some of them labeled (3-5), have total currents of the order $(5 - 10) \times 10^{11} A$. There is virtually no partition with clearly non-neutralized total current that is far from the AR’s PILs. We conclude, therefore, that the intensely flaring NOAA AR 10930 includes strong non-neutralized currents *only* where opposite-polarity flux-tube footprints are close enough to interact, that is, in proximity to PILs.

NOAA AR 10930 as a whole has a net current $I_{net} = (8 \pm 1.6) \times 10^{11} A$. With much stronger I_+ and I_- ($\pm[80 - 90] \times 10^{11} A$), the AR has a total current imbalance $\mathcal{I}_{imb} \simeq 0.036$.

This is more than an order of magnitude smaller than the magnetic flux imbalance of the AR, $\mathcal{F}_{\text{imb}} \simeq 0.4$. Consequently, NOAA AR 10930 as a whole can be considered current-balanced. This being said, the non-neutrality factor $\mathcal{I}_{\text{nn}}^{\pm} \simeq 0.80$, so $\mathcal{I}_{\text{nn}}^{\pm} \gg \mathcal{I}_{\text{imb}}$. As a result, besides strong non-neutrality in the AR, there is a large degree of coherence in the sense of electric current for each polarity: in particular, $\sim 80\%$ of partitions of a given polarity show a given sense of electric current (positive/negative current for negative/positive magnetic polarities). This opposite current-sense preference per polarity achieves an overall current-balanced AR so that non-neutralized currents of opposite polarities approximately close onto each other.

4.2. NOAA AR 10940

The flux-partitioned vertical magnetic field of NOAA AR 10940 is depicted in Figure 5a. Here we identified a total of $N = 297$ partitions, of which $p = 156$ show positive polarity and $n = 141$ show negative polarity. The average vertical current densities for each partition via the integral and the differential calculation are shown in Figures 5c and 5d, respectively, and are compared in Figure 5b. For this flare-quiet AR the average current densities are generally smaller than those of the flaring NOAA AR 10930. As expected, the differential J_z slightly overestimates the electric current density. From Figure 5b, $(J_z)_{\text{integral}} \sim 0.93(J_z)_{\text{differential}}$ (black line).

Important quantitative differences between NOAA ARs 10930 and 10940 are revealed, however, when the total currents of partitions are plotted for NOAA AR 10940: Figure 6a provides these currents in random order. The peak partition current here barely exceeds 3×10^{11} A that is more than an order of magnitude smaller than the respective peaks in NOAA AR 10930 (Figure 4a). Of the 297 identified partitions, 51 survive the significance test of equations (5). Of them, only 10 have total currents in excess of 10^{11} A. These partitions are all close to the weak, loosely formed PIL of the AR (Figure 6b). We conclude therefore, that (i) the flare-quiet NOAA AR 10940 also includes non-neutralized electric currents, albeit much weaker than those of the flaring NOAA AR 10930, and (ii) these weaker, non-neutralized currents are also found exclusively along the AR’s weaker PIL. It appears that the stronger (more flux-massive) the PIL, the more intense the non-neutralized currents it involves.

NOAA AR 10940 as a whole has a net current $I_{\text{net}} = (3.8 \pm 1.7) \times 10^{11}$ A, comparable to that of NOAA AR 10930, although the total currents I_+ and I_- are substantially smaller here ($\pm[10 - 15] \times 10^{11}$ A). The total current imbalance in the AR is $\mathcal{I}_{\text{imb}} \simeq 0.063$, ~ 4.5 times smaller than the magnetic flux imbalance $\mathcal{F}_{\text{imb}} \simeq 0.28$. Moreover, the non-neutrality factor $\mathcal{I}_{\text{nn}}^{\pm} \simeq 0.40$, so $\mathcal{I}_{\text{nn}}^{\pm} > \mathcal{I}_{\text{imb}}$. This degree of coherence in NOAA AR 10940 is half that

of the flaring NOAA AR 10930: different polarities show a significantly weaker preference in a given sense of electric currents.

Summarizing our findings, (i) NOAA AR 10940 as a whole can be characterized current-balanced, just like NOAA AR 10930, (ii) NOAA AR 10940 includes much weaker total currents than NOAA AR 10930, (iii) *both* NOAA ARs 10940 and 10930 involve non-neutralized current patterns flowing *exclusively* along their PILs, with the ones for the flare-quiet AR 10940 (that has a much weaker PIL) being more than an order of magnitude weaker than those of the flaring AR 10930, and (iv) NOAA AR 10940 is much less coherent (a factor-of-two difference) in terms of preference of electric-current sense per polarity, compared to NOAA AR 10930.

4.3. Dependence of results on partitioning threshold and varying spatial resolution

To obtain the results of §§4.1 and 4.2 we used a fixed, arbitrarily chosen threshold $B_{z_{thres}} = 100\text{ G}$ for the magnetic-flux partitioning and we took advantage of the high spatial resolution of Hinode’s SOT/SP magnetograms. To complete the analysis, we investigate the role of both the arbitrary $B_{z_{thres}}$ and the spatial resolution in our findings.

4.3.1. Varying partitioning threshold

First, we vary the value of $B_{z_{thres}}$ from 100 G to 1000 G and perform the same analysis as in §§4.1 and 4.2. We find that non-neutralized currents in both ARs continue to accumulate in the partitions identified in Figures 4 and 6, that is, close to the PILs of the ARs. In Figure 7 we show this behavior for NOAA AR 10930. In Figure 7a, the black curve indicates the fraction of the total (unsigned) magnetic flux of the AR that is represented by the partitioning for each $B_{z_{thres}}$ -value. Understandably, as more flux is left out of the partitioning for increasing $B_{z_{thres}}$, this fraction decreases. The magnetic flux imbalance \mathcal{F}_{imb} and the total current imbalance \mathcal{I}_{imb} for various $B_{z_{thres}}$ are shown with blue and red curves, respectively. For all $B_{z_{thres}}$, \mathcal{I}_{imb} is always 5-40 times smaller than \mathcal{F}_{imb} , regardless of the value of $B_{z_{thres}}$. Therefore, irrespectively of $B_{z_{thres}}$, NOAA AR 10930 includes non-neutralized current patterns close to its PILs but stays current-balanced globally. The non-neutrality factor \mathcal{I}_{nn}^{\pm} is substantial at all times ($\gtrsim 0.8$) and increases nearly monotonically for increasing $B_{z_{thres}}$. Therefore, we can safely conclude that $\mathcal{I}_{imb} \ll \mathcal{I}_{nn}^{\pm} \sim 1$ so the two different polarities in NOAA AR 10930 have both strong non-neutralized currents and a clear preference of sense

of electric currents, independently of $B_{z_{thres}}$.

In Figure 7b the blue curves show I_+ , for the positive-polarity partitions, and I_- for the negative-polarity ones, while the red curve shows the net current I_{net} . That $I_+ < 0$ and $I_- > 0$ indicates a predominantly left-handed, counterclockwise twist in the AR. Notice also that $|I_+|$ and $|I_-|$ tend to decrease for increasing $B_{z_{thres}}$. This indicates that non-neutralized currents become weaker if stronger, less interacting, fields are chosen for partitioning. Indeed, moving to thresholds $B_{z_{thres}}$ from several hundred G to 1 kG , we exclude some parts of the PILs of the AR. Regardless, the total current balance of the AR does not depend sensitively on $B_{z_{thres}}$: $|I_{net}|$ is always $\sim 3.5 - 4$ times smaller than $|I_+|$ and $|I_-|$.

The same analysis on NOAA AR 10940 is depicted in Figure 8. Because of the much weaker currents involved, increasing $B_{z_{thres}}$ in this case leads to more striking quantitative changes: for $B_{z_{thres}}$ ranging between 400 G and 800 G the current imbalance \mathcal{I}_{imb} increases to ~ 0.5 but still remains smaller than the respective flux imbalance \mathcal{F}_{imb} that ranges between 0.5 and 0.6 for the same $B_{z_{thres}}$ -range (Figure 8a). For $B_{z_{thres}} > 800\text{ G}$, \mathcal{I}_{imb} decreases significantly to reach ~ 0.2 at $B_{z_{thres}} = 1000\text{ G}$. Apparently the combination of weak total currents (Figure 8b) and a strongly imbalanced, inhomogeneous magnetic flux distribution where the one or the other polarity is favored for different $B_{z_{thres}}$ -values is the reason for these effects. The non-neutrality factor \mathcal{I}_{nn}^\pm initially increases and remains high at ~ 0.7 until $B_{z_{thres}} \simeq 600\text{ G}$, thereafter decreasing significantly to reach a value ~ 0.4 . At all times, though, $\mathcal{I}_{nn}^\pm > \mathcal{I}_{imb}$. The polarity currents I_+ and I_- (Figure 8b) peak at $\sim 20 \times 10^{11}\text{ A}$, ~ 5 times smaller than those in NOAA AR 10930. Their magnitudes also decrease for increasing $B_{z_{thres}}$ and this causes I_{net} , and hence \mathcal{I}_{imb} , to change significantly. Nonetheless, it would be biased to claim that whether NOAA AR 10940 is globally current-balanced depends on the value of $B_{z_{thres}}$. For reasonable values of this threshold, sufficient to keep a reasonably balanced representation of both polarities in the partitioning, the flare-quiet NOAA AR 10940 has an overall current-balanced structure, includes non-neutralized currents along its PIL, and shows some preference in a given sense of current for each polarity, similarly to its flaring counterpart NOAA AR 10930. However, this preference is much weaker than in the flaring AR, as are the non-neutralized current patterns NOAA AR 10940 involves.

4.3.2. Varying spatial resolution

We now study the impact of changing spatial resolution to the current patterns of the two ARs. We first bin each magnetogram using different sampling factors and then we re-calculate the subsequent current patterns using the analysis of §3 and keeping a fixed $B_{z_{thres}} = 100\text{ G}$ in all cases. For NOAA ARs 10930 and 10940 the results are summarized in

Tables 1 and 2, respectively.

For both ARs, we reach the following conclusions:

- (1) Decreasing the spatial resolution causes a decrease in the number of the identified partitions and a subsequent decrease in the number of partitions that include non-neutralized currents, that is, those satisfying the significance criteria of Equations (5). For the coarsest spatial resolution (pixel size $\sim 2.5''$) both NOAA ARs 10930 and 10940 include only three partitions. The identification of fewer partitions for coarser spatial resolution occurs because the morphological properties of the photospheric magnetograms - where partitioning relies - are suppressed or smoothed out when the resolution is reduced.
- (2) Decreasing the spatial resolution leads to a decrease in the total current magnitudes $|I_+|$ and $|I_-|$. Even in this case, however, strong non-neutralized current patterns in the flaring NOAA AR 10930 are easily discernible. This is not the case for NOAA AR 10940, whose current magnitudes fall almost within the uncertainty margins ($\sim 10^{11}$ A) for pixel sizes equal to $\sim 1.3''$ and $\sim 2.5''$. That NOAA AR 10930 seems to largely maintain its strong non-neutralized currents around its PILs even for very coarse resolution justifies previous studies that advocate for non-neutralized currents with much lower-resolution magnetograms (Leka et al. 1996; Semel & Skumanich 1998; Wheatland 2000; Falconer 2001). Our results differ from those of Wilkinson et al. (1992) who did not find compelling evidence of non-neutralized current patterns in the flaring NOAA AR 2372.
- (3) Regarding the ARs' overall current balance, Table 1 suggests that NOAA AR 10930 remains current-balanced regardless of spatial resolution. For all cases, \mathcal{F}_{imb} is 5 - 25 times larger than \mathcal{I}_{imb} . NOAA AR 10940 also appears current-balanced except in case the pixel size becomes $\geq 1.3''$. Then, $\mathcal{I}_{imb} \sim \mathcal{F}_{imb}$ but with very weak I_+ and I_- . These weak, insignificant currents practically invalidate any conclusions about \mathcal{I}_{imb} .
- (4) Regarding the non-neutrality factor \mathcal{I}_{nn}^\pm , it appears that binning consistently *increases* the coherence of each polarity in terms of sense of electric currents. This is the case for both ARs, although the results are somewhat mired in case of the flare-quiet NOAA AR 10940, where $\mathcal{I}_{imb} \sim \mathcal{I}_{nn}^\pm$ for coarser pixel sizes, due to the much weaker - and hence more uncertain - currents involved.

Briefly, we conclude that varying the partitioning threshold and/or altering the spatial resolution does not affect our findings of (i) non-neutralized current patterns along PILs, and (ii) globally current-balanced ARs. Only very restrictive partitioning or very coarse

spatial resolution can affect these findings, and only for flare-quiet ARs lacking tight, well-organized PILs. Large partitioning thresholds or severe binning can cause artifacts, such as the disappearance of these weak PILs. PILs, however, are parts of the “topological skeleton” of ARs (Bungey et al. 1996), which means that they are topologically stable features. As such, at least the strongest of them will survive, regardless of thresholding or smoothing. This study shows that non-neutralized current patterns are exclusively related to PILs; apparently the stronger the PIL, the more intense the non-neutralized currents it involves. If well-formed PILs cannot disappear due to thresholding or binning, their currents cannot disappear under these actions, either.

5. Physical implications of our results

We now attempt to establish a qualitative connection between our findings and the observed evolution along well-formed PILs. A crucial aspect of this evolution is magnetic shear. Shear is *invariably* formed along PILs (e.g., Falconer et al. 1997; Yang et al. 2004) with the effect being more pronounced in stronger PILs. Pending confirmation with larger active-region samples, this work also implies that non-neutralized electric currents are also stronger in stronger PILs. A connection between non-neutralized currents and magnetic shear, therefore, appears plausible.

Another notable finding of this study is that partitions of the same polarity tend to have the same sense of non-neutralized currents. This is reflected in the non-neutrality factor $\mathcal{I}_{\text{nn}}^{\pm}$ that is ~ 1 for the eruptive NOAA AR 10930, despite the large number (hundreds) of partitions for each polarity. The same result in the same active region was recently reported by Ravindra et al. (2011). A similar effect, but at a clearly smaller degree, occurs for the non-eruptive NOAA AR 10940. This coherence of electric currents, more pronounced in more compact ARs with stronger PILs, must be of sub-photospheric origin. Indeed, numerous simulations of magnetic flux emergence, (e.g., Tortosa-Andreu & Moreno-Insertis 2009; Archontis & Hood 2010; Cheung et al. 2010), all start from a single flux tube with a given twist in the convection zone. Upon emergence in the photosphere, the flux tube undergoes substantial fragmentation. We show here that in the course of such a fragmentation electric currents largely retain their sub-photospheric sense. Strong PILs likely indicate a strongly twisted, perhaps braided (López Fuentes et al. 2003), coherent sub-photospheric flux tube, while weak PILs suggest a loosely formed sub-photospheric tube with only the necessary coherence to survive its emergence in the solar atmosphere.

But how, and why, does magnetic shear occur along intense PILs? For NOAA AR 10930, studied here, Su et al. (2007) concluded that the observed shear is due to sunspot

rotation and the east-west motion of the emerging positive-polarity sunspot just south of the negative-polarity main sunspot of the AR. The main PIL of the AR is between these two spots (Figure 1). Here we reveal additional information, namely that strong and systematic non-neutralized currents are formed along the PIL and only there. These currents suggest that the Lorentz force may be the most natural cause of shear. This is already suggested in several works: Manchester & Low (2000) analytically showed that the *tension* component of the Lorentz force can cause shear in an undulated emerging flux tube. This result was numerically demonstrated by Manchester (2001). Manchester et al. (2004) modeled a Lorentz-force-driven shear with a gradient ranging from photosphere to corona, supporting earlier observations of differential shear in active regions (Schmieder et al. 1996). A systematic modeling of the Lorentz-force-driven shear that demonstrates a coupling between sub-photospheric and atmospheric magnetic fields was performed by Manchester (2007). This author demonstrated by MHD flux emergence simulations that a gradient in the axial magnetic field (along the PIL) during the emergence of an Ω -loop is the cause of the Lorentz force that further causes shear flows leading to magnetic shear. These flows have an amplitude of about half the local Alfvén speed, hence increasing from the photosphere to the corona. These results were supported by Fang et al. (2010) who further found that U -loops may be formed along PILs, in agreement with Tortosa-Andreu & Moreno-Insertis (2009). In the sub-photospheric part of U -loops, however, they showed that the Lorentz force can unshear the magnetic field lines, contrary to the situation in and above the photosphere.

In an effort to provide a heuristic explanation of the shear-generating Lorentz force \mathbf{F} and its physical connection to non-neutralized currents, we write \mathbf{F} in terms of magnetic tension and pressure (Jackson 1962), i.e.,

$$\mathbf{F} = \frac{1}{4\pi}[(\mathbf{B} \cdot \nabla)\mathbf{B} - \frac{1}{2}\nabla B^2] . \quad (15)$$

The azimuthal component F_φ of the Lorentz force in cylindrical coordinates (r, φ, z) is given by

$$F_\varphi = \frac{1}{4\pi} \left[B_r \frac{\partial B_\varphi}{\partial r} + \frac{1}{2r} \frac{\partial (B_\varphi^2 - B^2)}{\partial \varphi} + B_z \frac{\partial B_\varphi}{\partial z} + \frac{B_r B_\varphi}{r} \right] . \quad (16)$$

All terms in Equation (16) are due to magnetic tension, with the exception of the term $-(1/(2r))\partial B^2/\partial \varphi$ that is due to magnetic pressure.

We first assume a pair of undisturbed, twisted flux-tube footprints embedded in field-free, plasma-filled space (Figure 9a). Obviously there is no strong PIL interfacing between the footprints in this case. We further ignore the (generally nonzero) azimuthal Lorentz force in the flux-tube interior and focus on the outer edges of the tube (dark blue and red rings) where sheath currents reside, and we seek the azimuthal Lorentz force F_φ acting in

this area. There, the two terms of F_φ depending on the radial field component B_r vanish because the field has to be largely azimuthal, with a weaker vertical component B_z , to ensure a divergence-free magnetic field vector. After some algebra, Equation (16) on the footprint edges becomes

$$F_\varphi \simeq \frac{B_z}{4\pi} \left(-\frac{1}{r} \frac{\partial B_z}{\partial \varphi} + \frac{\partial B_\varphi}{\partial z} \right) . \quad (17)$$

Notice that *all* derivatives in Equation (17) are due to magnetic tension. Azimuthal symmetry in the undisturbed case implies $\partial/\partial\varphi \sim 0$ and since B_z is weak and vanishing at the edge of the flux tubes, $F_\varphi \simeq 0$ from Equation (17) on the interface between the flux tube and the field-free space. On this interface it is the *radial* component of the Lorentz force that becomes important. This component, driven by magnetic pressure, will force the flux tube's cross-section to increase as much as the outside plasma pressure allows. The formation of roughly azimuthally symmetric - hence fully neutralized within a given polarity - cross-field sheath (return) currents will protect the flux tube from disintegrating. As Parker (1996b) demonstrated, there are no net currents injected in this situation.

We now assume a pair of interacting flux-tube footprints that deform due to this interaction, forming a strong PIL between them (Figure 9b). The field will still have to be predominantly azimuthal on the interface in this case, too, so Equation (17) can still be used. However, (i) the vertical field component B_z is non-vanishing any more; in fact, it can be quite strong along both sides of the PIL, and (ii) enhanced, PIL-localized azimuthal field gradients build-up in the deformation area, even in this simplified, axially symmetric (with respect to the PIL) case. These gradients preferentially enhance sheath currents along the PIL. These currents cannot be neutralized any more within a given polarity. Evidently, then, $F_\varphi \neq 0$ along the PIL (but not *on* it, because $B_z = 0$ there) unless the two terms in the parenthesis of Equation (17) cancel each other. This resulting azimuthal Lorentz force is purely due to magnetic tension. Cancellation of the derivative terms may conceivably happen, but in general it is not the cause, and it is certainly not true in case of asymmetries in the magnetic flux distribution within a given footprint. Nonzero azimuthal Lorentz force will cause shearing motions along the PIL that will further give rise to magnetic shear, as demonstrated in numerical simulations. Qualitatively, this result is similar for all *interacting* opposite-polarity flux tubes.

In the actual solar photosphere, the plasma β -parameter is high enough for MHD to compete with the hydrodynamics of the non-magnetized plasma. This dense plasma, therefore, should exhibit an *inertia* to the action of the Lorentz force that can only be overcome locally, where strong fields give rise to powerful azimuthal Lorentz forces (Equation (17)). An intuitive PIL field strength that, if exceeded, should allow F_φ to move the plasma, is the *equipartition* value B_{eq} needed for $\beta = 1$. Assuming typical photospheric values for convec-

tive flows and mass density, or for number density and the effective temperature, one finds $B_{eq} \sim (200 - 1400) G$, with a mean $B_{eq} \simeq 800 G$. In NOAA AR 10930 the field strength around the PIL always exceeds 1.5 kG and, in many cases, it is higher than 2 kG (Figure 1). In this case it is clear that $\beta < 1$ in the PIL area, hence F_φ should be powerful enough to move the plasma. In NOAA AR 10940 the PIL field strength ranges between a few hundred G to $\lesssim 1.5$ kG. In this case, therefore, despite some non-neutralized currents, the azimuthal Lorentz force may not be able to shear plasma and magnetic field considerably. This rough interpretation qualitatively agrees with the observational facts for both studied ARs.

In a symmetric case such as the one of Figure 9b, Equation (17) clearly implies an *opposite* orientation of F_φ in the two sides of the PIL that leads to an opposite sense of shear flows. In case of strong asymmetries, however, the competition of the two tension terms in the parenthesis may result in the *same* sign of F_φ in the two PIL sides, and hence in a *similar* sense of shear flows. Asymmetries can be simply thought of as severe flux imbalance and/or different field morphologies of the partitions deformed along the PIL. For the studied NOAA AR 10930, for example, inspection of continuum and magnetogram movies implies that velocity shear mainly acts in the counterclockwise direction in *both* sides of the PIL. Figure 1b shows clearly that the PIL area is strongly asymmetric. Even in case of similar shear orientation, however, asymmetries lead to strong velocity gradients across the PIL that give rise to strong relative motions in the two sides of the PIL. Albeit in a more complicated manner, therefore, the end result of strongly asymmetric shear flows is qualitatively similar with that of the symmetric case. The directionality of the shear is determined by the direction of B_φ that is due to the dominant sense of twist in the flux tube. The consistency of the shear-flow orientation for the lifetime of the PIL corroborates our findings that there indeed exists a dominant sense of twist in interacting opposite-polarity flux tubes.

The proposed mechanism of Lorentz-force-driven shear along PILs is, of course, qualitative - careful quantitative studies are necessary for all aspects of it to be clarified at sufficient detail. The study of Török & Kliem (2003) first showed numerically that as soon as shearing motions are generated in the PIL area, non-neutralized currents inevitably build up in the corona. Shear in that study was generated by placing bipolar flux concentrations – twisted by photospheric vortex flows – progressively closer to each other: the closer the concentrations, the larger their non-neutralized total current. Further, Török et al. (2011) recently analyzed the evolution of electric currents in an emerging flux-rope simulation. As predicted earlier by Longcope & Welsch (2000), these authors also found that the electric current in the coronal part of the emerging flux rope is, indeed, essentially non-neutralized, although the physical mechanism underlying this effect has yet to be clarified. Works like the above substantiate our findings for non-neutralized currents in active-region PILs while our proposed mechanism, at work in case opposite-polarity photospheric flux concentrations

approach close enough to interact, provides a physical context for this effect.

6. Summary and Conclusions

Using solar magnetic field measurements of the highest available spatial resolution we have studied in detail the electric current patterns of the photospheric magnetic configurations in two solar active regions; a flaring/eruptive, and a flare-quiet one. Our main objective was to determine whether emerging and/or evolving active regions inject significant non-neutralized electric currents in the solar atmosphere through the photospheric boundary. We show that such currents are injected solely and exclusively along the photospheric magnetic PILs that accompany the dynamical formation and evolution of active regions. In our limited sample of two active regions we find that stronger PILs imply more intense non-neutralized currents. This result is robust and insensitive to magnetic-field thresholding and the spatial resolution of the studied magnetograms, but has to be confirmed by future studies with larger active-region samples.

Despite current non-neutrality in particular locations within active regions, our study confirms that active regions as a whole are current-balanced magnetic structures. This means that non-neutralized currents injected on one side of a PIL are roughly counter-balanced by non-neutralized currents of the opposite sense that are developed on the other side of the PIL.

An additional finding, in agreement with recent results (Ravindra et al. 2011), is the coherence in the sense of electric currents within a given polarity. We have quantified the effect by means of a dimensionless parameter dubbed the global non-neutrality factor (Equation (14)). We find that this effect is more pronounced in the eruptive active region we study, but it is also present in the non-eruptive region (Figures 4a; 6a and Tables 1, 2), despite the considerable flux fragmentation in the photosphere. We conclude that this effect is of sub-surface origin, which stands in agreement with the results of multiple numerical simulations that show substantial fragmentation of a *single* buoyant flux tube in realistic simulations of emerging active regions (e.g., Cheung et al. 2010).

Our findings seem to put a nearly twenty-year-old debate to rest: amidst claims ranging between no injection of net electric currents in the solar atmosphere, per Parker’s (1996b) isolated flux-tube picture (see Introduction), and injection of net currents in each and every magnetic flux emergence episode, we demonstrate that injection of significant net currents *does occur* but it is as rare – or as frequent – as the appearance of intense PILs in the solar photosphere. In this case only, Parker’s assumption of isolated flux tubes breaks down and

Melrose’s (1991, 1995) proposition of non-neutralized photospheric currents becomes valid. It is obviously beyond the scope of this work to argue on the detailed nature of the sub-photospheric origin of these currents (i.e., the $[\mathbf{E}, \mathbf{J}]$ - vs. the $[\mathbf{B}, \mathbf{u}]$ -paradigm). However, we argue that strong non-neutralized currents occur exclusively in case of emerging magnetic footprints of opposite polarities that are close enough to interact, i.e. to “feel” each other and deform as a result of this interaction. Deformation implies preferential enhancement of return currents sheathing these flux tubes at the deformed areas. Because sheath currents are perpendicular to the axes of the tubes, these perturbations imply the exertion of a Lorentz force that, via magnetic tension, generates shear along the PIL, in terms of both shear flows and magnetic shear. The more enhanced the sheath currents developed in more flux-massive, tight PILs, the stronger the Lorentz force and the resulting shear, provided that the magnetic field strength in the PIL area is greater than the equipartition value (plasma $\beta < 1$), so that the Lorentz force can overcome the hydrodynamic inertia and move the plasma (§5).

The direction of shear flows is typically opposite in the two sides of the PIL (Equation (17)). The magnetic shear angle reflects the sense of twist of the interacting flux tubes: for the studied NOAA AR 10930, negative magnetic polarities associate to positive (non-neutralized) currents and vice-versa (Figures 3, 4) – this implies a left-handed sense of twist in the region. An opposite situation (right-handed twist) in a similar field configuration would imply an opposite shear orientation in the region. Notice that the main PIL of NOAA AR 10930 is also strongly asymmetric, leading to predominant counterclockwise, but similarly asymmetric, shear motions on both sides of the PIL. We explain this effect in §5. These asymmetric flows roughly lead to the same end result as in the case of oppositely oriented shear flows due to significant relative motions in the two sides of the PIL.

We conclude by emphasizing the need for more detailed qualitative and quantitative studies of the causal sequence *interacting flux tubes [PIL] – non-neutralized electric currents – Lorentz force – shear*. Such studies may shed new light into the physics of eruption initiation and pre-eruption active-region evolution. Besides simulations, the role of the Lorentz force appears to become evident even from observations, albeit in post-eruption situations (Hudson et al. 2008; Fisher et al. 2012). Moreover, the coherence of non-neutralized currents per polarity, stemming from a common sub-photospheric origin of these currents, directly relates to a *dominant* sense of twist in eruptive active regions. This, in addition, may translate to a dominant sense of magnetic helicity in eruptive active regions, as demonstrated by previous (e.g., Nindos & Andrews 2004; LaBonte et al. 2007; Georgoulis et al. 2009) and recent (e.g., Tziotziou et al. 2012) works. Undoubtedly, much remain to be revealed, but efforts should focus on putting together as many pieces of the solar eruption puzzle as possible in the most meaningful physical interpretation possible. We intend to undertake such efforts in future studies.

We are grateful to the anonymous referee for critical comments that have soundly improved the presentation of the analysis and results. MKG acknowledges the help of Manolis Zoulias in technical matters related to the preparation of the manuscript. This work has received partial support from the European Union’s Seventh Framework Programme (FP7/2007-2013) under grant agreement *n*^o PIRG07-GA-2010-268245. The contributions of VST and ZM were supported by NASA’s Living With a Star, Heliophysics Theory, and SR&T Programs.

REFERENCES

- Alissandrakis, C. E. 1981, *A&A*, 100, 197
- Archontis, V., & Hood, A. W. 2008, *ApJ*, 674, L113
- . 2010, *A&A*, 514, A56
- Balthasar, H. 2006, *A&A*, 449, 1169
- Barnes, G., Longcope, D. W., & Leka, K. D. 2005, *ApJ*, 629, 561
- Bernasconi, P. N., Rust, D. M., Georgoulis, M. K., & Labonte, B. J. 2002, *Sol. Phys.*, 209, 119
- Borrero, J. M., & Ichimoto, K. 2011, *Living Reviews in Solar Physics*, 8, 4
- Bruzek, A. 1967, *Sol. Phys.*, 2, 451
- Bungey, T. N., Titov, V. S., & Priest, E. R. 1996, *A&A*, 308, 233
- Cheung, M. C. M., Rempel, M., Title, A. M., & Schüssler, M. 2010, *ApJ*, 720, 233
- Ding, Y. J., Hong, Q. F., Hagyard, M. J., Deloach, A. C., & Liu, X. P. 1987, *Sol. Phys.*, 109, 307
- Falconer, D. A. 2001, *J. Geophys. Res.*, 106, 25185
- Falconer, D. A., Moore, R. L., Porter, J. G., Gary, G. A., & Shimizu, T. 1997, *ApJ*, 482, 519
- Fang, F., Manchester, W., Abbett, W. P., & van der Holst, B. 2010, *ApJ*, 714, 1649
- Fisher, G. H., Bercik, D. J., Welsch, B. T., & Hudson, H. S. 2012, *Sol. Phys.*, 277, 59

- Georgoulis, M. K. 2005, *ApJ*, 629, L69
- . 2012, *Sol. Phys.*, 276, 423
- Georgoulis, M. K., & LaBonte, B. J. 2004, *ApJ*, 615, 1029
- Georgoulis, M. K., LaBonte, B. J., & Metcalf, T. R. 2004, *ApJ*, 602, 446
- Georgoulis, M. K., Raouafi, N., & Henney, C. J. 2008, in *Astronomical Society of the Pacific Conference Series*, Vol. 383, *Subsurface and Atmospheric Influences on Solar Activity*, ed. R. Howe, R. W. Komm, K. S. Balasubramaniam, & G. J. D. Petrie , 107–+
- Georgoulis, M. K., Rust, D. M., Pevtsov, A. A., Bernasconi, P. N., & Kuzanyan, K. M. 2009, *ApJ*, 705, L48
- Georgoulis, M. K., Tziotziou, K., & Raouafi, N.-E. 2012, *ArXiv e-prints*
- Harvey, J. W. 1969, PhD thesis, UNIVERSITY OF COLORADO AT BOULDER.
- Henney, C. J., Keller, C. U., Harvey, J. W., Georgoulis, M. K., Hadder, N. L., Norton, A. A., Raouafi, N., & Toussaint, R. M. 2009, in *Astronomical Society of the Pacific Conference Series*, Vol. 405, *Astronomical Society of the Pacific Conference Series*, ed. S. V. Berdyugina, K. N. Nagendra, & R. Ramelli, 47–+
- Howard, R., & Stenflo, J. O. 1972, *Sol. Phys.*, 22, 402
- Hudson, H. S., Fisher, G. H., & Welsch, B. T. 2008, in *Astronomical Society of the Pacific Conference Series*, Vol. 383, *Subsurface and Atmospheric Influences on Solar Activity*, ed. R. Howe, R. W. Komm, K. S. Balasubramaniam, & G. J. D. Petrie , 221
- Jackson, J. D. 1962, *Classical Electrodynamics*, ed. N. Y. Wiley
- Kosugi, T., et al. 2007, *Sol. Phys.*, 243, 3
- LaBonte, B. J., Georgoulis, M. K., & Rust, D. M. 2007, *ApJ*, 671, 955
- Leka, K. D., Barnes, G., Crouch, A. D., Metcalf, T. R., Gary, G. A., Jing, J., & Liu, Y. 2009, *Sol. Phys.*, 260, 83
- Leka, K. D., Canfield, R. C., McClymont, A. N., & van Driel-Gesztelyi, L. 1996, *ApJ*, 462, 547
- Lites, B. W., Elmore, D. F., Seagraves, P., & Skumanich, A. P. 1993, *ApJ*, 418, 928

- Lites, B. W., Elmore, D. F., & Streander, K. V. 2001, in *Astronomical Society of the Pacific Conference Series*, Vol. 236, *Advanced Solar Polarimetry – Theory, Observation, and Instrumentation*, ed. M. Sigwarth, 33–+
- Lites, B. W., et al. 2008, *ApJ*, 672, 1237
- Livingston, W., & Harvey, J. 1969, *Sol. Phys.*, 10, 294
- Longcope, D. W., & Welsch, B. T. 2000, *ApJ*, 545, 1089
- López Fuentes, M. C., Démoulin, P., Mandrini, C. H., Pevtsov, A. A., & van Driel-Gesztelyi, L. 2003, *A&A*, 397, 305
- Manchester, W., & Low, B. C. 2000, *Physics of Plasmas*, 7, 1263
- Manchester, IV, W. 2001, *ApJ*, 547, 503
- . 2007, *ApJ*, 666, 532
- Manchester, IV, W., Gombosi, T., DeZeeuw, D., & Fan, Y. 2004, *ApJ*, 610, 588
- Martinez Pillet, V., Lites, B. W., & Skumanich, A. 1997, *ApJ*, 474, 810
- McClymont, A. N., Jiao, L., & Mikic, Z. 1997, *Sol. Phys.*, 174, 191
- Melrose, D. B. 1991, *ApJ*, 381, 306
- . 1995, *ApJ*, 451, 391
- Metcalf, T. R., Jiao, L., McClymont, A. N., Canfield, R. C., & Uitenbroek, H. 1995, *ApJ*, 439, 474
- Metcalf, T. R., et al. 2006, *Sol. Phys.*, 237, 267
- Murray, M. J., Hood, A. W., Moreno-Insertis, F., Galsgaard, K., & Archontis, V. 2006, *A&A*, 460, 909
- Nindos, A., & Andrews, M. D. 2004, *ApJ*, 616, L175
- Parker, E. N. 1972, *ApJ*, 174, 499
- . 1979, *Cosmical magnetic fields: Their origin and their activity* (Oxford University Press), pp. 207–208
- . 1996a, *ApJ*, 471, 489

- . 1996b, *ApJ*, 471, 485
- . 2004, *Physics of Plasmas*, 11, 2328
- . 2007, *Conversations on Electric and Magnetic Fields in the Cosmos* (Princeton University Press), p. 42
- Pizzo, V. J. 1986, *ApJ*, 302, 785
- Press, W. H., Teukolsky, S. A., Vetterling, W. T., & Flannery, B. P. 1992, *Numerical recipes in FORTRAN. The art of scientific computing*
- Ravindra, B., Venkatakrisnan, P., Tiwari, S. K., & Bhattacharyya, R. 2011, *ApJ*, 740, 19
- Sakurai, T. 1982, *Sol. Phys.*, 76, 301
- Schmidt, H. U. 1964, *NASA Special Publication*, 50, 107
- Schmieder, B., Demoulin, P., Aulanier, G., & Golub, L. 1996, *ApJ*, 467, 881
- Schuessler, M. 1979, *A&A*, 71, 79
- Semel, M., & Skumanich, A. 1998, *A&A*, 331, 383
- Socas-Navarro, H. 2005, *ApJ*, 631, L167
- Stenflo, J. O. 1973, *Sol. Phys.*, 32, 41
- Su, Y., et al. 2007, *PASJ*, 59, 785
- Su, Y. N., Golub, L., van Ballegooijen, A. A., & Gros, M. 2006, *Sol. Phys.*, 236, 325
- Tiwari, S. K., Venkatakrisnan, P., & Gosain, S. 2010, *ApJ*, 721, 622
- Török, T., Archontis, V., & Titov, V. S. 2011, *AGU Fall Meeting Abstracts*, C8
- Török, T., & Kliem, B. 2003, *A&A*, 406, 1043
- Tortosa-Andreu, A., & Moreno-Insertis, F. 2009, *A&A*, 507, 949
- Tziotziou, K., Georgoulis, M. K., & Raouafi, N.-E. 2012, *ArXiv e-prints*
- Venkatakrisnan, P., & Tiwari, S. K. 2009, *ApJ*, 706, L114
- Wang, H., Ewell, Jr., M. W., Zirin, H., & Ai, G. 1994, *ApJ*, 424, 436
- Wang, H., Jing, J., Tan, C., Wiegelmann, T., & Kubo, M. 2008, *ApJ*, 687, 658

Wang, J. 1999, *Fund. Cosmic Phys.*, 20, 251

Wheatland, M. S. 2000, *ApJ*, 532, 616

Wilkinson, L. K., Emslie, A. G., & Gary, G. A. 1992, *ApJ*, 392, L39

Yang, G., Xu, Y., Cao, W., Wang, H., Denker, C., & Rimmele, T. R. 2004, *ApJ*, 617, L151

Zhang, H. 2001, *ApJ*, 557, L71

Zirin, H. 1988, *Astrophysics of the sun* (Cambridge University Press), pp. 172–175

Zirin, H., & Wang, H. 1993, *Nature*, 363, 426

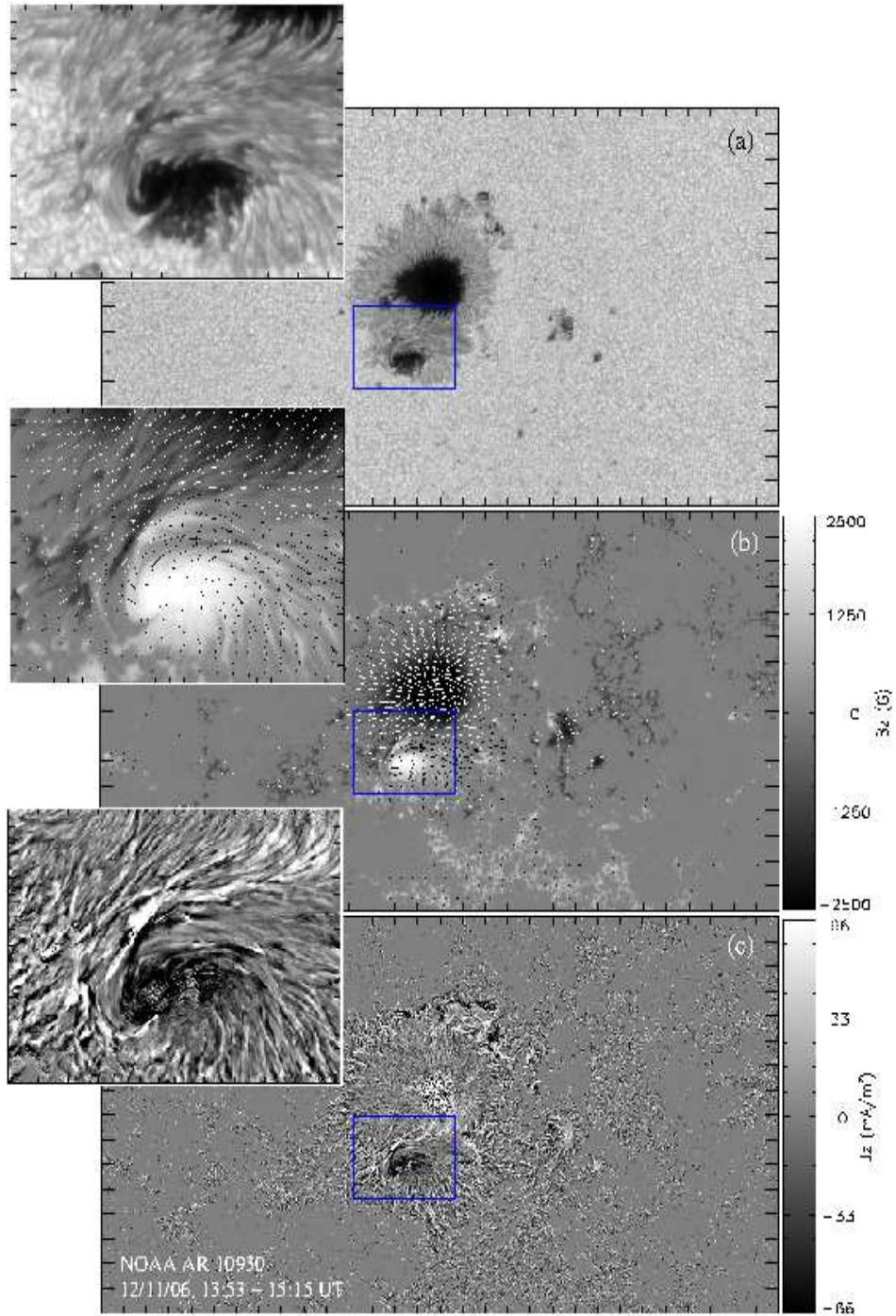


Fig. 1.— Views of NOAA AR 10930, observed by SOT/SP on 2006 December 12, at around 20:30 UT. (a) Continuum image of the active-region photosphere. (b) The corresponding photospheric magnetic field vector on the heliographic plane. A vector length equal to the tic mark separation corresponds to a horizontal field strength of 2000 G. (c) The corresponding

photospheric vertical electric current density. In all images, a part of the AR, enclosed by the blue boxes, has been expanded and shown in the insets. Tic mark separation for the full images is $10''$. Tic mark separation for the insets is $2''$. A vector length equal to the tic mark separation in the inset of b corresponds to a horizontal field strength of $1000 G$. North is up; west is to the right.

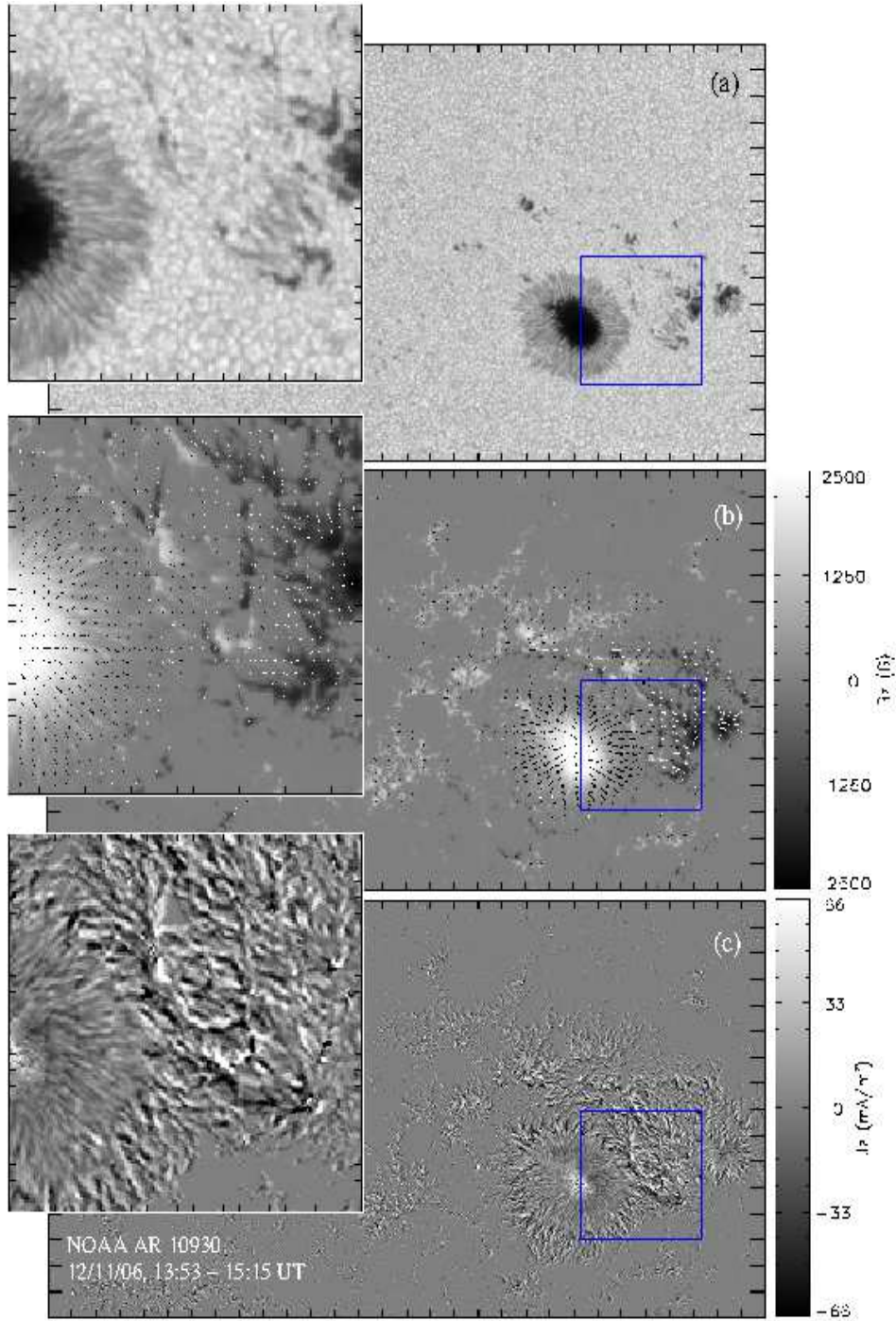


Fig. 2.— Same as Figure 1, but for NOAA AR 10940, observed by SOT/SP on 2007 February 2, around 01:50 UT. A vector length equal to the tic mark separation in the inset of b corresponds to a horizontal field strength of 1900 G. North is up; west is to the right.

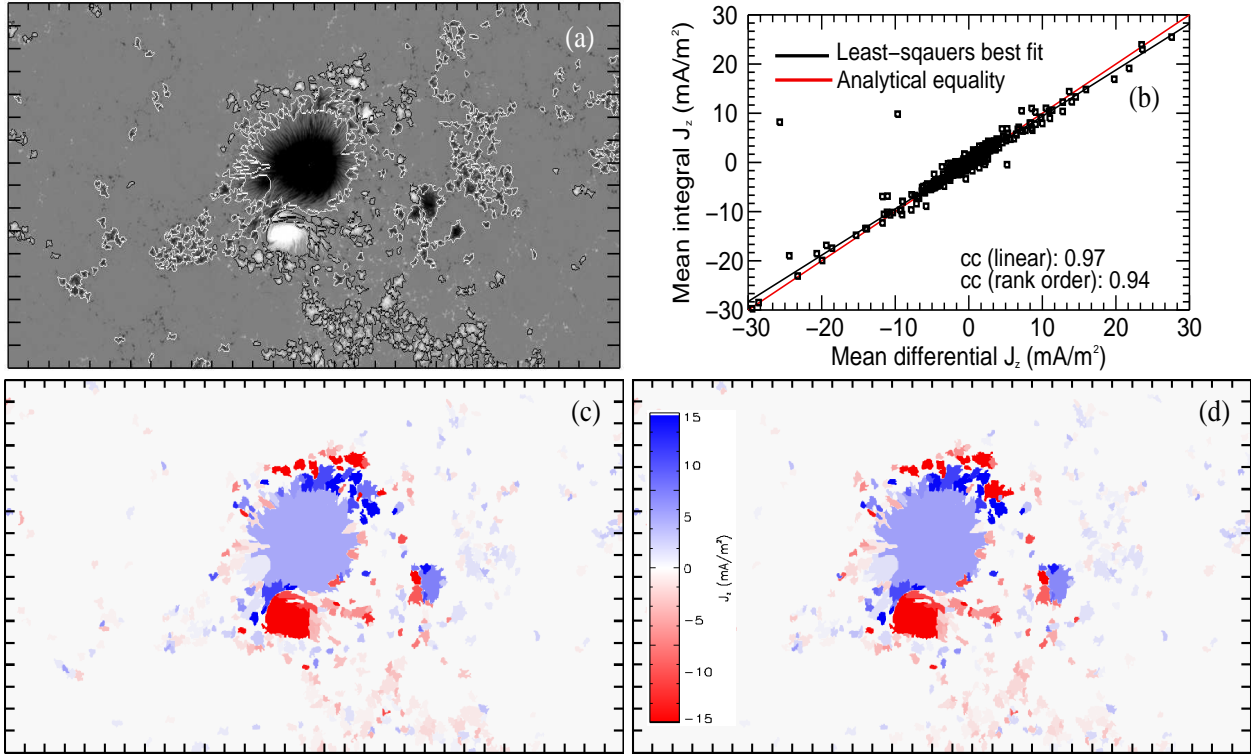


Fig. 3.— Flux and current partitioning of NOAA AR 10930. (a) The partitioned vertical magnetic field, saturated at ± 2000 G. Different partitions are indicated by their enclosing contours. (b) Comparison between the mean vertical electric current densities per partition, as calculated using the integral (shown in c) and the differential (shown in d) forms of Ampère’s law. Both current-density maps (c,d) are saturated at $\pm 15 \text{ mA}/\text{m}^2$. The linear (Pearson) and rank-order (Spearman) correlation coefficients (cc) between the two current density estimates are also given. Tic mark separation in all images is $10''$.

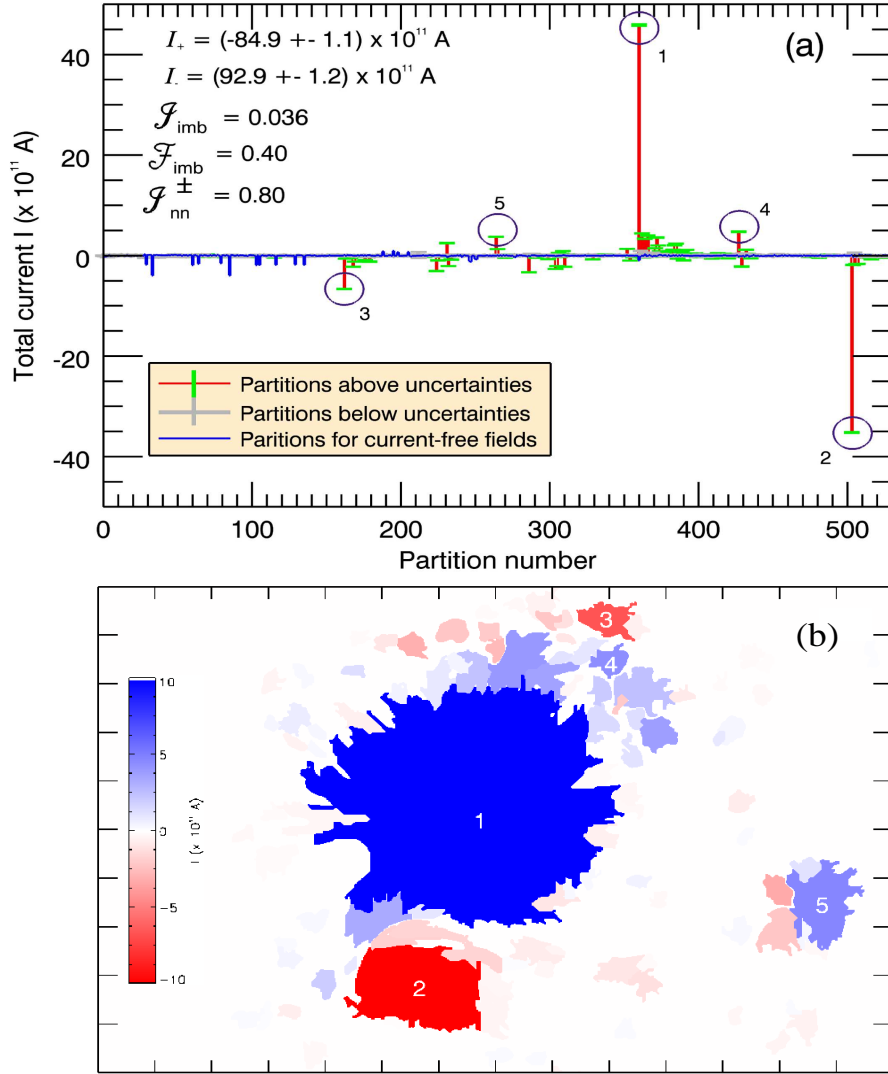


Fig. 4.— Total partition currents in NOAA AR 10930. (a) Total currents for each partition. Currents that satisfy the significance criteria of equations (5) are shown with red columns and green error bars. Five of the largest non-neutralized total currents are encircled and labeled (1-5). The total currents I_+ and I_- for positive- and negative-polarity partitions, respectively, the total current imbalance \mathcal{I}_{imb} , the magnetic flux imbalance \mathcal{F}_{imb} , and the non-neutrality factor $\mathcal{I}_{\text{nn}}^{\pm}$ are also given. (b) Detail of the active region showing the spatial distributions of the partitions that satisfy the criteria of equations (5). Different partitions are indicated by different shades of blue and red, according to their total current. Total currents are saturated at $\pm 10^{12}$ A. Partitions 1-5, with total currents corresponding to the five currents identified in a, are also indicated. Tic mark separation is $10''$.

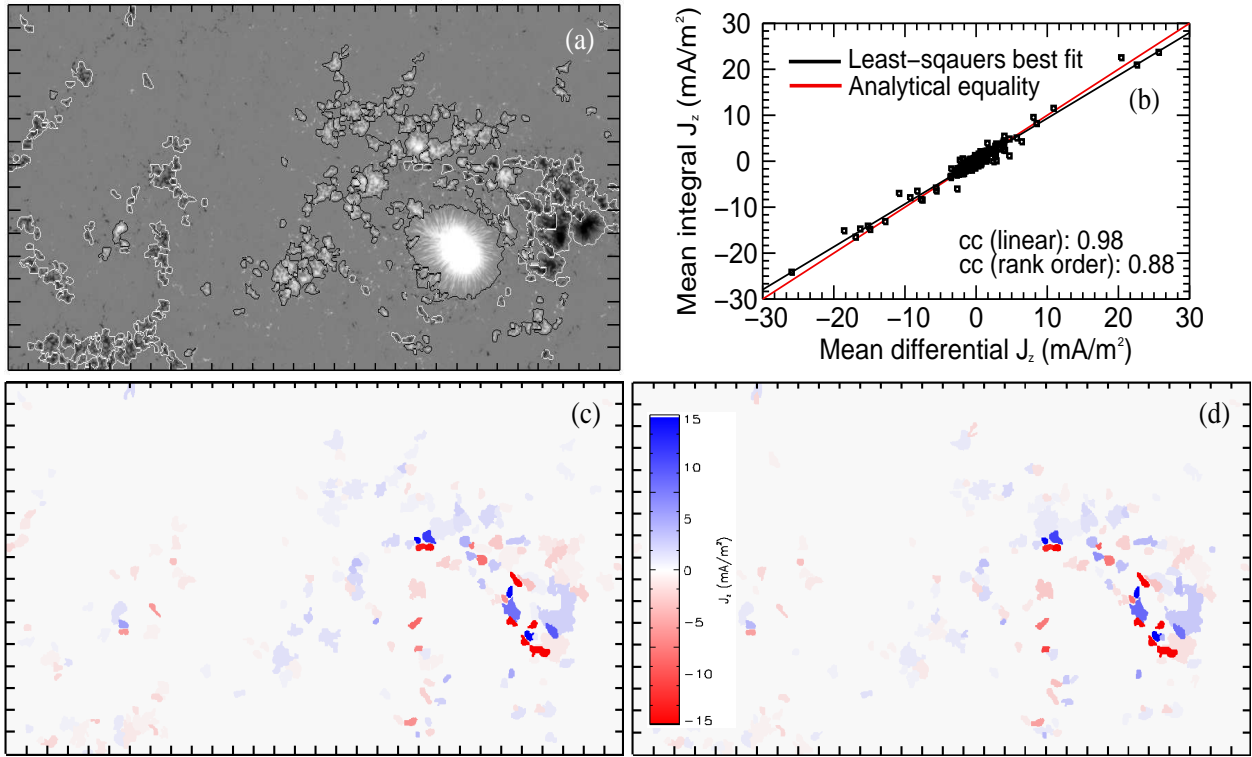


Fig. 5.— Same as Figure 3, but for NOAA AR 10940.

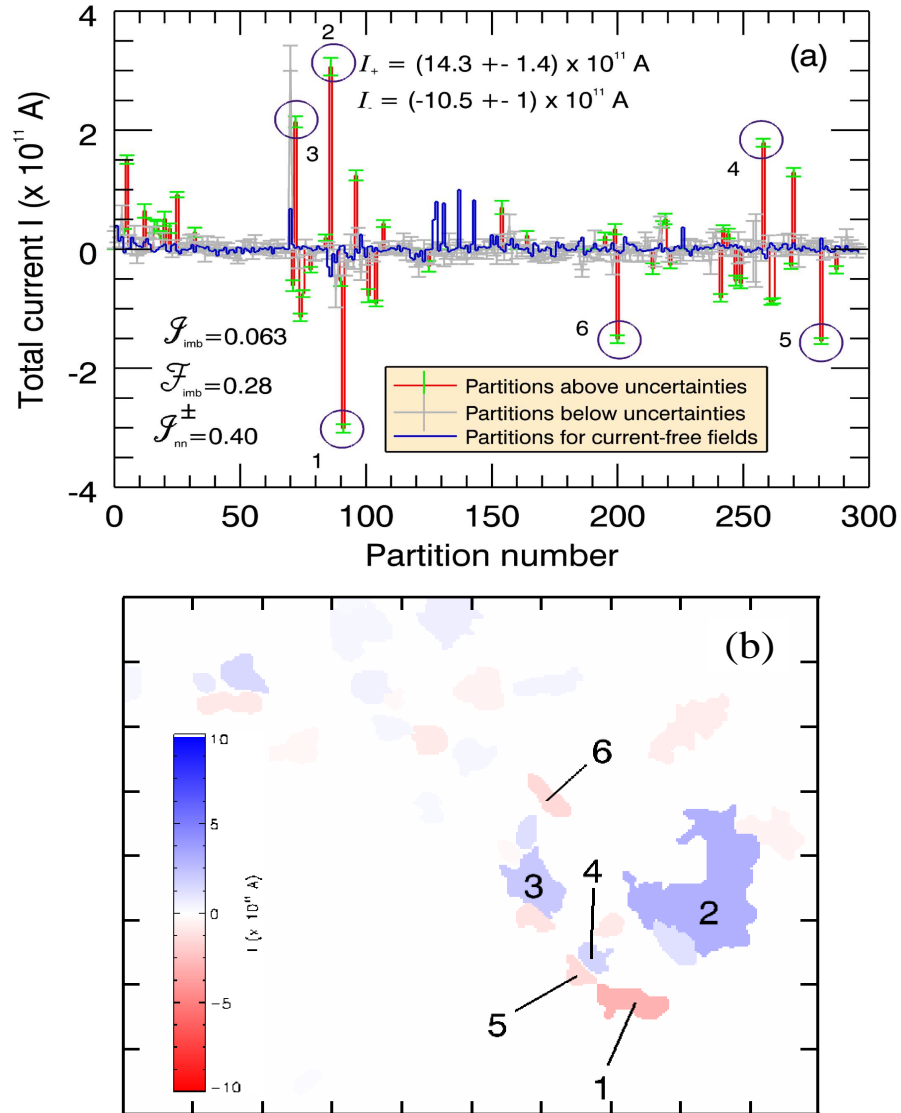


Fig. 6.— Same as Figure 4, but for NOAA AR 10940. Six partitions with the largest non-neutralized total currents are identified here.

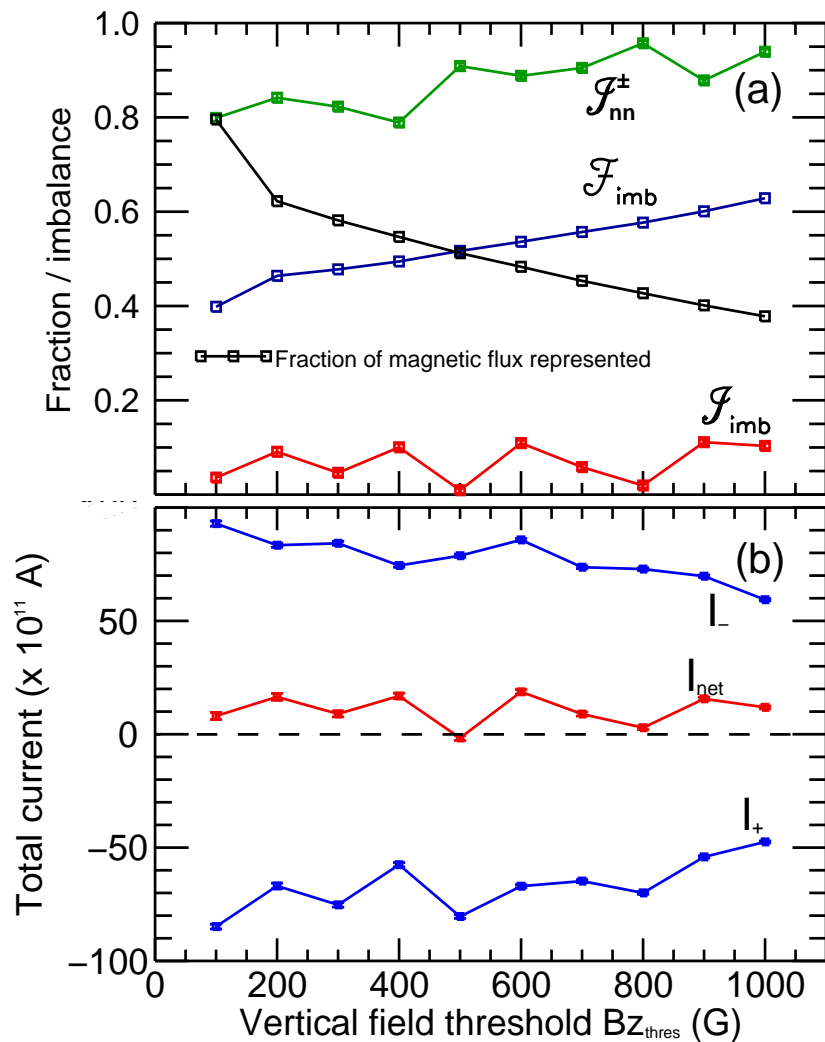


Fig. 7.— Total electric currents in NOAA AR 10930 for different partitioning thresholds $B_{z_{thres}}$. (a) Curves show the fraction of the magnetic flux represented by the partitioning (black), the total current imbalance \mathcal{I}_{imb} (red), the magnetic flux imbalance \mathcal{F}_{imb} (blue), and the current non-neutrality factor \mathcal{I}_{nn}^{\pm} (green) for each $B_{z_{thres}}$. (b) The total currents I_{+} and I_{-} for the positive and negative polarity, respectively (blue curves) and the net current I_{net} (red curve).

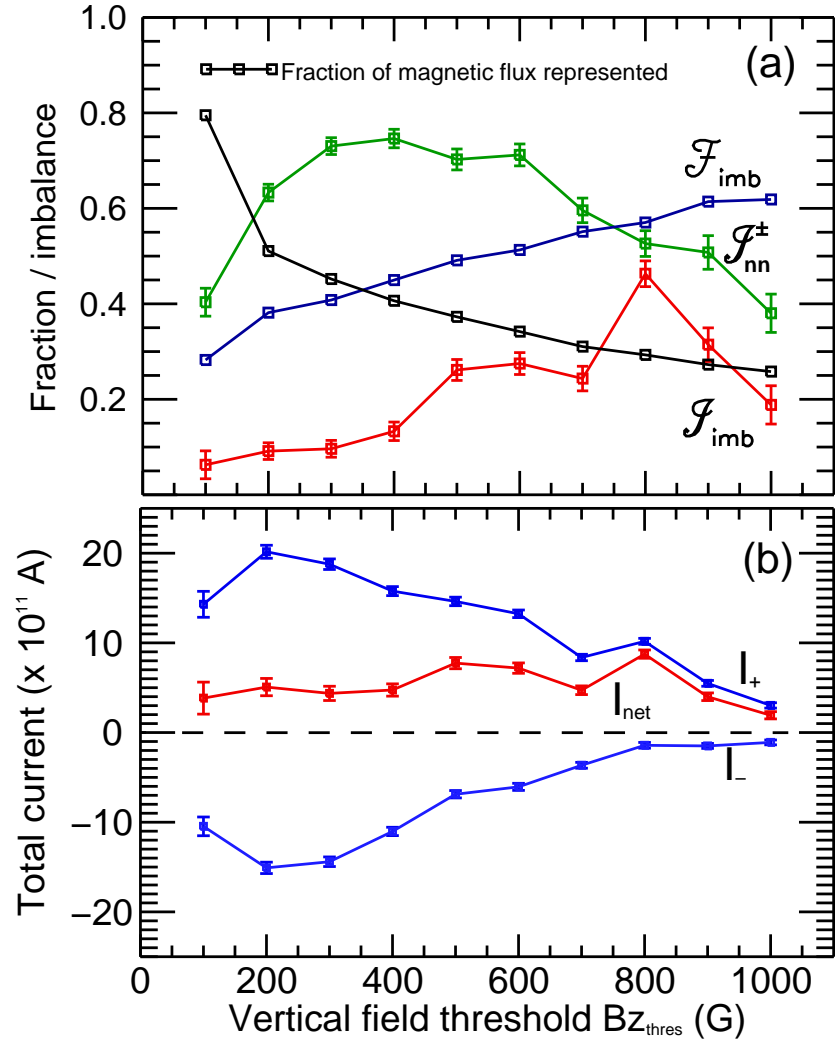


Fig. 8.— Same as Figure 7, but for NOAA AR 10940.

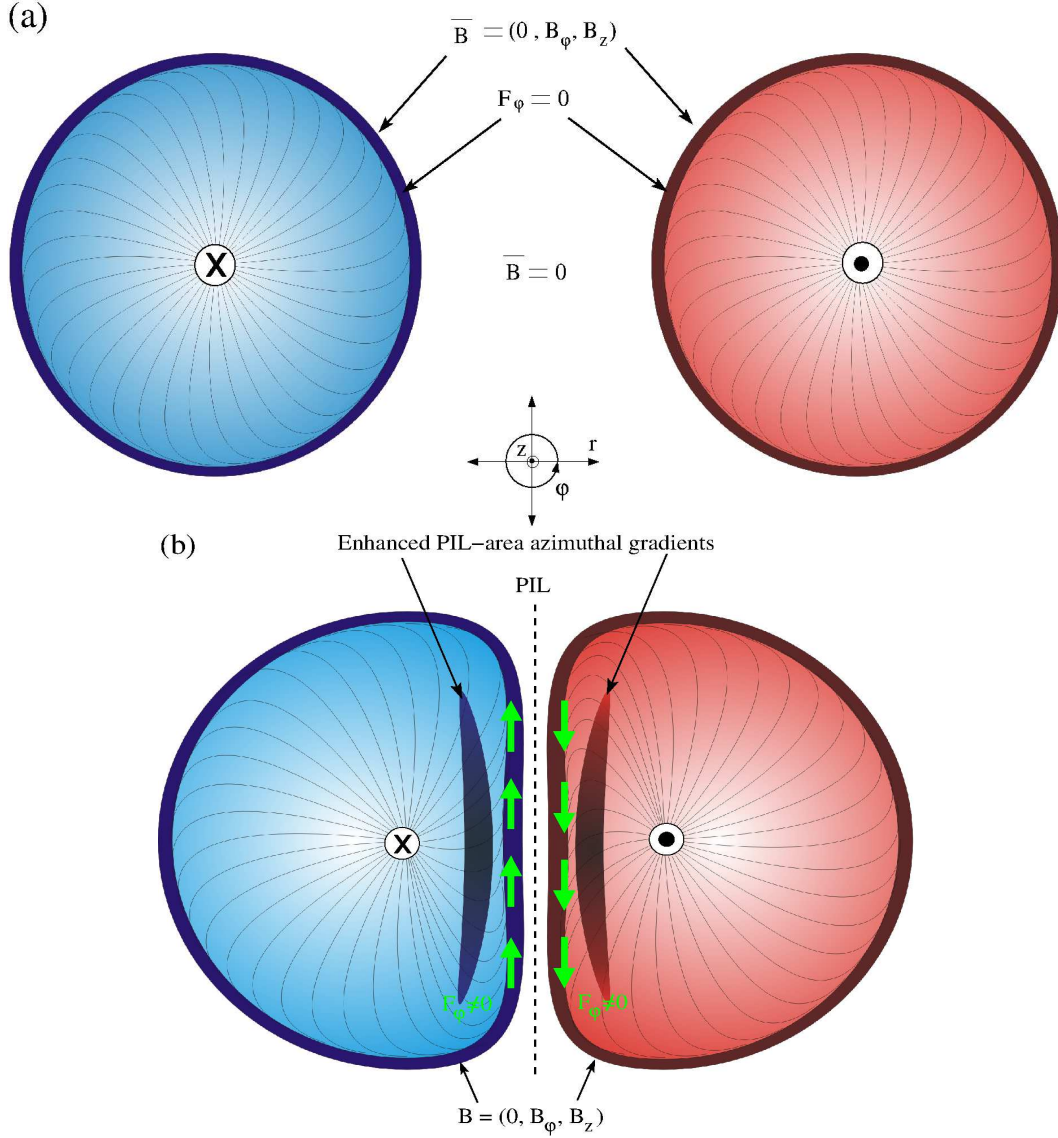


Fig. 9.— Simplified concept for the occurrence of shear-generating Lorentz forces along lower-boundary PILs in solar active regions. The situation is qualitatively similar for different altitudes, along the normal direction z , until the field becomes space-filling. (a) In case of non-interacting flux-tube footprints, hence no well-defined PILs, a lack of azimuthal gradients within and on the interface between the flux tube and the field-free space inhibits a shearing (azimuthal) Lorentz force F_φ . (b) In case of interacting, deformed flux tubes, inhomogeneous azimuthal gradients are formed (dark shapes), preferentially enhancing sheath currents along the PIL (dashed line) that become non-neutralized within a given polarity and give rise to an azimuthal, shearing Lorentz force F_φ in the PIL area. In both panels, the field polarity is denoted at the center of each footprint, while red- and blue-color gradients suggest the

gradient of \mathbf{B} . Spiral curves denote twist in the flux tube, and hence the presence of an azimuthal field B_φ . Each footprint is enclosed by its sheath currents ($\sim \nabla B \times \mathbf{B}$ - dark red and blue rings) for the flux tube to maintain coherence.

Pixel size (<i>arcsec</i>)	N	N_{nn}	I_+ ($\times 10^{11}$ A)	I_- ($\times 10^{11}$ A)	I_{net} ($\times 10^{11}$ A)	\mathcal{I}_{imb}	$\mathcal{I}_{\text{nn}}^{\pm}$	\mathcal{F}_{imb}
0.1585	531	120	-84.9 ± 1.1	92.9 ± 1.2	8.1 ± 1.6	0.036	0.799	0.398
0.317	449	76	-86.1 ± 0.8	89.7 ± 0.9	3.7 ± 1.1	0.018	0.867	0.447
0.634	65	19	-58.7 ± 0.6	70.3 ± 0.6	11.6 ± 0.8	0.086	0.967	0.583
1.268	12	6	-47.9 ± 0.4	57.2 ± 0.6	9.3 ± 0.7	0.089	1.000	0.678
2.536	3	2	-38.8 ± 0.6	50.9 ± 0.6	12.1 ± 0.8	0.132	0.978	0.665

Table 1: Effect of varying spatial resolution on the total currents of NOAA AR 10930; N is the total number of partitions, N_{nn} is the number of non-neutralized partitions. The pixel size has been modified by binning the original Hinode SOT/SP magnetogram of the AR. Shown are the total currents per polarity (I_+ , I_-), the net current (I_{net}), the total-current imbalance (\mathcal{I}_{imb}), the current non-neutrality factor ($\mathcal{I}_{\text{nn}}^{\pm}$), and the magnetic-flux imbalance (\mathcal{F}_{imb}).

Pixel size (<i>arcsec</i>)	N	N_{nn}	I_+ ($\times 10^{11}$ A)	I_- ($\times 10^{11}$ A)	I_{net} ($\times 10^{11}$ A)	\mathcal{I}_{imb}	$\mathcal{I}_{\text{nn}}^{\pm}$	\mathcal{F}_{imb}
0.317	297	45	14.3 ± 1.5	-10.46 ± 1	3.8 ± 1.8	0.063	0.403	0.282
0.634	50	9	11.5 ± 0.5	-7.2 ± 0.5	4.2 ± 0.7	0.156	0.681	0.474
1.268	10	2	7.0 ± 0.6	-1.2 ± 0.4	5.8 ± 0.7	0.514	0.640	0.581
2.536	3	1	3.9 ± 0.5	2.1 ± 0.5	6.0 ± 0.7	0.580	0.663	0.541

Table 2: Same as Table 1 but for NOAA AR 10940.